UNIVERSITAT
POLITÈCNICA
DE VALÈNCIA

_ TELECOM ESCUELA
TÉCNICA VLC SUPERIOR
DE INGENIERÍA DE
TELECOMUNICACIÓN

NOVEL PHOTONIC SWITCHING COMPONENTS WITH NON-VOLATILE RESPONSE FOR TELECOM APPLICATIONS

Alba Vicente Olmo

Tutor: Pablo Sanchis Kilders

Trabajo Fin de Grado presentado en la Escuela Técnica Superior de Ingenieros de Telecomunicación de la Universitat Politècnica de València, para la obtención del Título de Graduado en Ingeniería de Tecnologías y Servicios de Telecomunicación

Curso 2018-19

Valencia, 3 de julio de 2019

Escuela Técnica Superior de Ingeniería de Telecomunicación

Universitat Politècnica de València

Edificio 4D. Camino de Vera, s/n, 46022 Valencia

Tel. +34 96 387 71 90, ext. 77190

www.etsit.upv.es

VLC/
CAMPUS
VALENCIA, INTERNATIONAL
CAMPUS OF EXCELLENCE

EMAS
Gestión
ambiental
verificada
REG.NO. ES-CV-000030

Resumen

El objetivo del Trabajo Fin de Grado (TFG) es el diseño de nuevos componentes fotónicos de conmutación que presenten una respuesta óptica no-volátil y sean integrables en tecnología fotónica de silicio. La plataforma tecnológica de fotónica de silicio se utiliza actualmente en el desarrollo de circuitos integrados fotónicos. En este trabajo, se estudiará la integración de materiales con una respuesta óptica no-volátil, tales como el GST o GSST, en circuitos integrados de silicio y se llevará a cabo el diseño de diversos componentes de conmutación analizando y evaluando sus prestaciones. Además, se analizará y validará el montaje experimental para abordar la validación experimental de los componentes diseñados. El acceso a dichos componentes resulta de gran interés para nuevas aplicaciones emergentes en el campo de las telecomunicaciones tales como los circuitos fotónicos reconfigurables, redes de conmutación ópticas o nuevos esquemas de computación neuromórfica.

Resum

L'objectiu del TFG ès el disseny de nous components fotònics de commutació que presenten una resposta òptica no-volàtil i siguen integrables en tecnologia fotònica de silici. La plataforma tecnològica de fotònica de silici s'utilitza actualment en el desenvolupament de circuits integrats fotònics. En aquest treball, s'estudiarà la integració de materials amb una resposta òptica no-volàtil, com ara el GST o GSST, en circuits integrats de silici i es durà a terme el disseny de diversos components de commutació analitzant i avaluant les seues prestacions. A més, s'analitzarà i validarà el muntatge experimental per abordar la validació experimental dels components dissenyats. L'accés a aquests components resulta de gran interès per a noves aplicacions emergents en el camp de les telecomunicacions com ara els circuits fotònics reconfigurables, xarxes de commutació òptiques o nous esquemes de computació neuromòrfica.

Abstract

The goal of this Bachelor’s thesis is to design novel photonic switching components with non-volatile optical response integrable with the silicon photonics technology. The silicon photonics platform is currently employed in the development of Photonic Integrated Circuits. In this work, the integration of materials having a non-volatile optical response, like GST or GSST, in silicon photonics circuits will be examined and the design and analysis of diverse switching components will be carried out. Moreover, the designed components will be validated by an experimental set-up. Development of these components is pertinent for emerging applications in the telecommunications field such as reconfigurable photonics, optical switching networks or new neuromorphic computing.

Table of Contents

1. Introduction

1.1. Photonic Integration

Photonics is the science of generation, detection and manipulation of light or other forms of energy whose quantum unit is the photon. Derived from the Greek word *phos* (*light*), it was first coined in the 1960s after the invention of the laser and was greater used once fiber-optics were deployed by telecommunication operators. This research field intends to use light to carry out tasks that typically were performed by electronic systems.

The term "integrated photonics" refers to the integration of waveguides and photonic devices as individual structures on a common planar substrate. These circuits can transmit and process light in an analogue way to how electronic integrated circuits work with electronic signals. The main goal of integrated photonics is the integration and miniaturization of optical systems which will enable the commercial fabrication of Photonic Integrated Circuits (PICs) [1]. Optical systems have advanced in such way that they are now prominent in long-distance communications through optical fibers. With the ceaseless increase in the required link bit rates and the reduction in costs of optical technologies, photonics is also gradually replacing electronics in short distance interconnections [2], leading to what may be an all-optical communication system in the future.

The fundamental reason for using photons instead of electrons relates to the higher frequency of light, which translates into a very large bandwidth. The larger the bandwidth, the greater the amount of information that can be transported and managed. Electronic systems are limited by physical restraints: as the frequency of an electrical signal increases, the impedance of the conductor through which it is travelling also rises, thereby reducing the propagation capacities. Consequently, communications based on electrical signals requiring high transmission rates can only be achieved in short distances. On the other hand, optical signals travel through non-conductive dielectric media at much higher frequencies than the ones used in electrical transmission. where materials can be treated as transparent to light. In this range of frequencies, wavelengths are relatively short (0.5-2 μm), which enables the fabrication of very small devices.

The working principle behind integrated photonic circuits is similar to that associated with fiber optics. As a result of the total internal reflection phenomenon, light is confined in a medium whose refractive index is bigger than the one of the surrounding material. High refractive index media can be used to build waveguides that transport optical signals between different points [1].

Over past decades, integrated photonics advanced at a slower pace than integrated electronics, particularly in terms of integration density [3]. Nevertheless, exploration of materials like III-V compounds (GaAs, InP, InGaAs [4]), ferroelectrics ($LiNbO_3$, $BaTiO_3$), polymers and silicon (Si) and silica (SiO_2) has paved the way to a promising future for this field of study.

1.2. Silicon Photonics platform

The first optical channel waveguides were demonstrated in the mid-1970s using a broad variety of materials. LiNbO$_3$ was the most widely used, allowing for low-loss channel waveguides with high efficiency electro-optic effect. Alongside, dielectrics like polymers, glasses, silica on silicon and semiconductors like indium phosphide (InP) and gallium arsenide (GaAs) were being researched and deemed to be suitable for photonic circuits. Today, the choice between materials depends on the specific application, due to the huge difference in properties they show: LiNbO$_3$ is mainly used for modulators, InP and GaAs for lasers and photodetectors and SiO$_2$ for passive devices. Nonetheless, these materials are difficult to integrate together and are not convenient for mass production. In order for integrated photonics to evolve to the degree of electronics, an ultra-high level of integration that allows for a high-volume production at a low cost is needed.

Silicon photonics is one of the most promising platforms for this purpose, having multiple advantages over other substrate materials. Most remarkable are the compatibility with the already well-developed CMOS technology and the high index contrast between Si-SiO$_2$. The former leads to scalability and cost reduction and the latter to a higher optical confinement and, therefore, to smaller devices [5]. Moreover, a unique advantage of silicon photonics derives from the possibility of integration of electronics and photonics on the same chip, reaching submicron dimensions and bending radius as low as few micrometers.

Connection of optical fibers to integrated circuits may also be low-loss and a wide range of passive devices have been demonstrated. In addition, active components such as lasers, which cannot be directly fabricated in silicon, could be heterogeneously integrated in the silicon platform [6]. Table 1 shows the main advantages and drawbacks of silicon in photonic integration.

Advantages	**Disadvantages**
CMOS compatibility.	Lacks efficient light emission and no electro-optic effect.
High refraction index contrast (Si-SiO$_2$) that allows smaller footprints.	The small size makes coupling to fiber optics harder.
Transparent to light in 1.3-1.6μm.	No detection in 1.3-1.6μm.

Table 1. Advantages and disadvantages of silicon for photonic integration.

One of the challenges of silicon photonics yet to be overcome is the lack of a silicon-based light source, due to the not-efficient electroluminescence of this material. Current commercial products use external III-V based-lasers that need to be coupled to the integrated circuit. Even though this approach may be adequate for some applications, the development of an on-chip light source with low power consumption is desirable.

Additionally, other crucial elements in silicon photonics are the packaging and coupling of fiber optics. Coupling losses are critical and must be minimized. Alignment is necessary and is hindered by the size difference between fibers and typical submicrometer waveguides [5]. The potential level of integration and mass-production at a low cost of optoelectronic devices in silicon opens up a range of possible applications. Significant improvements in terms of integration density, speed and power consumption could be achieved. Some of the fields that would benefit from silicon photonics include telecommunications, optical interconnects, sensor technologies, signal processing, neural networks, optical storage, gaming, supercomputers. [7].

1.3. Non-volatile optical response materials

Phase-Change Materials (PCMs)

Even though the Si platform displays low-loss optical transmission, its moderate range of optical properties makes it necessary to draw attention to hybrid silicon devices that integrate Si with other active materials [8].

Phase-Change Materials have been widely studied due to their energy storage capacity: they are classified as latent heat storage units because of their capability of accumulating and releasing latent heat. For their application in photonics, the most interesting characteristic of PCMs is the fast and reversible switch between two atomic states, that can be thermally, optically or electrically triggered. Optical properties of these materials change drastically between states and transition times lie in the range of nanoseconds. The use of femtosecond pulses has also been demonstrated [9]. The state change is reversible, with more than 100,000 cycles with stable composition [10]. Some PCMs also possess the so-called "self-holding feature": the states are non-volatile, meaning there is no need for continuous power supply to maintain them. Under ambient conditions, the alleged thermal stability is of decades [11]. Table 2 shows a summary of these properties, that make PCMs best suited for integrated photonic applications.

Properties of Phase-Change Materials	
Drastic change of optical properties between states.	State transition can be performed with short and low energy pulses.
State change is fast and reversible.	Intermediate states are achievable.
Non-volatile states, no need of continuous supply of power.	Scalability, integrability with silicon.

Table 2. Summary of properties of PCMs.

The most common PCMs used in photonic applications are transition metal oxides (VO_2, V_4O_7, $NdNiO_3$, $PrNiO_3$) and chalcogen-based alloys (GeTe, $GeSb_2Te_4$, $Ge_2Sb_2Te_5$). Fig. 1 shows the complex refractive index of GeTe, $GeSb_2Te_4$, $Ge_2Sb_2Te_5$ compared to two ordinary semiconductors ($AgInTe_2$, InSb) [11].

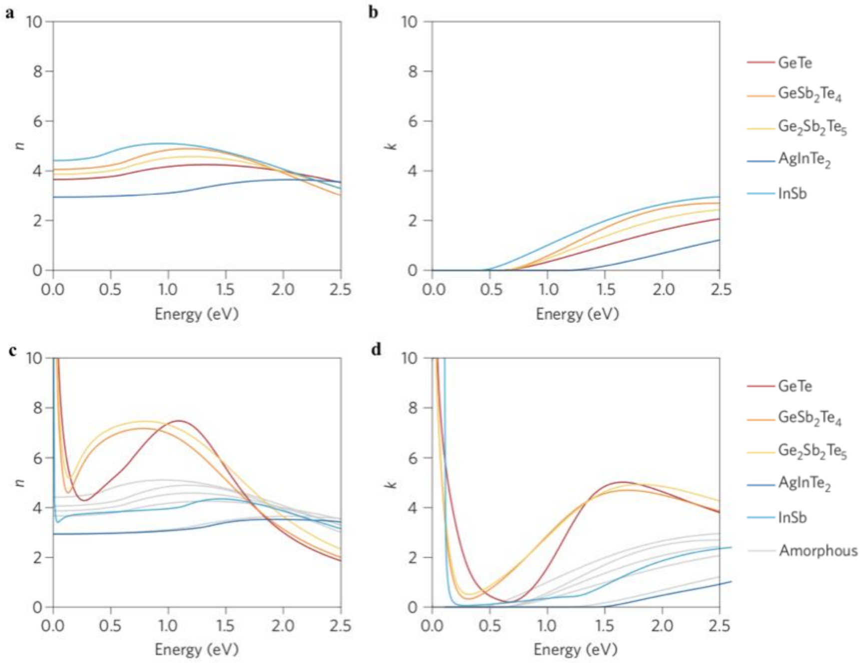

Fig. 1. Complex refractive index (*n*+*ki*) as a function of photon energy for the amorphous (**a,b**) and crystalline (**c,d**) states. Grey lines in c, d are the equivalent to the amorphous state, included for comparison [11].

The refractive index (both real and imaginary parts) of PCMs significantly increases in the crystalline phase. This is mainly due to a drastic variation of the chemical bonding. A high index contrast is an appealing property in integrated photonics as it allows for the implementation of smaller footprints. The most interesting feature is the fact that the state change can be controlled, and therefore, so can the optical properties, paving the way for switchable reconfigurable photonic devices [12]. By carefully controlling the energy and number of stimulating pulses, intermediate phases can be achieved, allowing for multi-level operations.

The potential applications of PCMs are wide, ranging from optical memories, reconfigurable logic, switching to neuromorphic and quantum computing. As such, future research into PCMs is deeply important and pertinent to a range of scientific disciplines.

Phase-Change Materials with non-volatile optical response

A common PCM is VO_2 (vanadium dioxide), an oxide which has the metal-to-insulator (MIT) property. VO_2 shows a large resistivity change (derived from the change in refractive index) between phases, with hysteresis at around 65ºC. This huge contrast is favourable to allow smaller active lengths and reduce the power consumption in comparison to other commonly used materials. The phase change can be electrically, optically or thermally driven. Although this is an appealing property, the states in VO_2 are volatile at room temperature, a common characteristic of transition metal oxide PCMs.

Therefore, VO_2 is not suitable for applications requiring static states (like non-volatile optical memories) but offers great utility in volatile applications such as modulation [8].

$Ge_2Sb_2Te_5$, also known as GST, is another typical PCM that had not been employed in silicon photonics until recently. It has proven to have better optical performance than VO_2 due to its non-volatile states. The material can be switched between an amorphous (aGST) and crystalline (cGST) state. Once the phase change is induced, the material will remain in that state indefinitely. Amorphization is achieved by heating the GST above melting temperature (~600ºC) followed by fast quenching. Crystallization is achieved by heating it above crystallization temperature (140ºC) but below melting one (546ºC) [13], [14]. GST is a highly absorptive material that can attenuate light's power significantly. It is not ideal to place GST directly on the light's path. Therefore, the typical implementation consists in depositing GST on top of a low-loss optical waveguide.

Fig. 2 shows a comparison of the complex refractive index of VO_2 and GST as a function of the wavelength for both states [8]. The main drawback of both VO_2 and GST is that they show excessive losses.

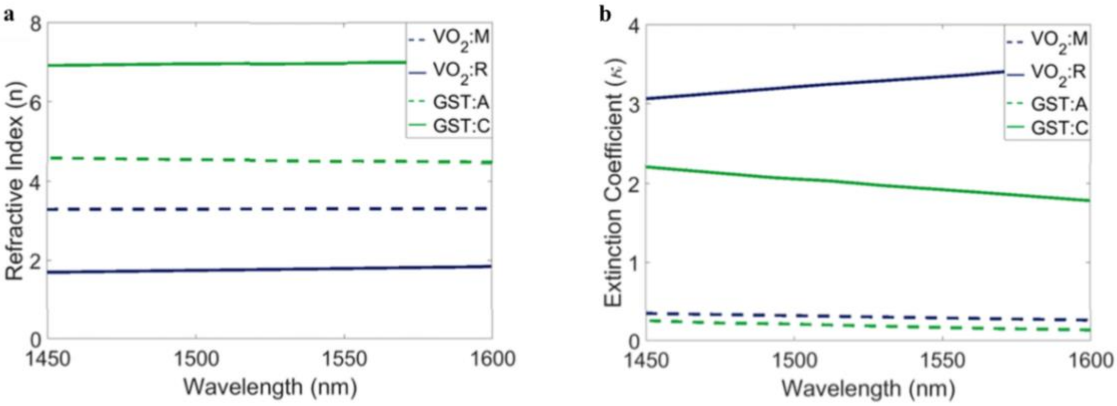

Fig. 2. **a)** Refractive index and **b)** extinction coefficient of GST in amorphous (GST:A) and crystalline (GST:C) states and VO_2 in monoclinic/insulator (VO_2:M) and rutile/metal (VO_2:R) states [8].

$Ge_2Sb_2Se_4Te_1$ (GSST) is a material derived from GST by partially replacing Te with Se. GSST suffers from significantly less attenuation compared to traditional PCMs. Fig. 3 compares the values of the complex refractive index of GST and GSST. We can see that at telecom wavelengths, GSST optical constants are considerable smaller.

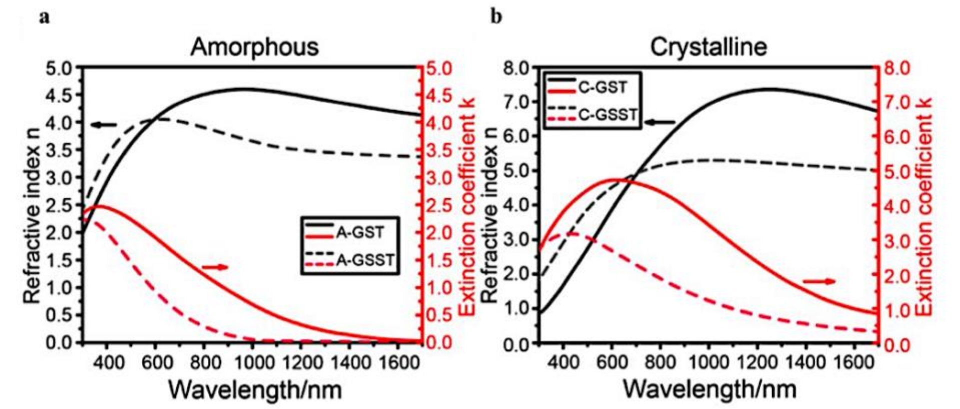

Fig. 3. Optical constants of a) amorphous and b) crystalline states of GST and GSST [15]. Black lines represent *n*, red lines represent *k*.

As a comparison example, we define a typical Figure of Merit (FOM) that is employed to quantify the impact of losses on the performance of an optical switch.

$$\text{FOM}=\frac{\Delta n}{k} \tag{1}$$

Where Δn and k represent the effective refractive index change upon state transition and the extinction coefficient, respectively. This FOM correlates with the attainable insertion losses (loss of signal power in the device) and extinction ratio (ratio between maximum and minimum signal power) of optical devices. In [16], the integration of GSST in Si photonic devices reported an exceptional FOM >900 at 1550 nm. This is 20 times larger than the corresponding of GST.

These materials are the most widely used PCMs. They offer a promising potential in producing broadband, with small footprint and low power consumption photonic devices.

1.4. Applications of devices with a non-volatile optical response

Reconfigurable photonics and switching

In a similar way to how the invention of FPGAs in 1985 opened up the field of applications of electronic circuits, the prospect of large-scale reconfigurable optical chips could unlock a significant number of applications [17] for the integrated photonics field. The application-specific PICs (ASPICs) are designed to carry out a task in an ideal way in terms of losses, consumption, footprint and number of components, which also implies a long development time and higher cost [18]. Reconfigurable Photonic Integrated Circuits (Reconfigurable PICs) would bring about larger flexibility, cost reduction and fault tolerance relative to APICs.

The unit structure of programmable photonic circuits is the optical switch. It can be implemented using different structures (e.g. directional couplers, Mach-Zehnder interferometers, micro-ring resonators). Most current optical switches are based on either the thermo-optic or electro-optic effects. Devices based on the former are usually characterized by a low speed and a high-power consumption. Devices based on the latter improve the speed but also suffer from a less efficient switching effect and thermal drift. These two switching mechanisms are volatile, thereby needing a continuous energy supply[19].

Phase-Change Materials, even if traditionally have not played a role in reconfigurable electronics, are proposed as a solution to these constraints. They are considered as suitable materials due to their already-mentioned characteristics: high refractive index contrast between states (allowing for stronger modulations, smaller footprints and less power consumption), self-holding feature, multi-state configuration and fast and reversible state transition. In addition, PCM-based integrated switches have already been successfully demonstrated [15], [19]-[20].

In [19], 1x2 and 2x2 switches are implemented using GST and directional couplers. The state of the switch (bar/cross) is determined by the state of the GST layer on top of one of the waveguides. In the 1x2 switch depicted in Fig. 4, when the GST layer is in the low-loss amorphous state, both structures match in phase and all the power is transferred from the input waveguide to the “cross” output. When in the crystalline state, the high attenuation present in GST guarantees minimal interaction between waveguides and the switch will turn to the bar state. The same concept is applied to develop the 2x2 switch seen in Fig. 5. The operation relies on the significant modification of the modes travelling through the three-waveguide system when GST transitions between states.

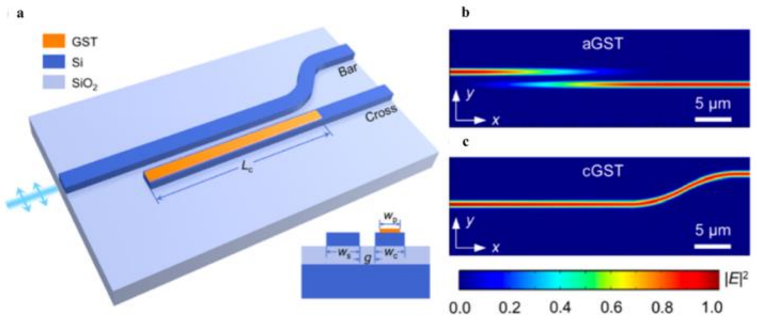

Fig. 4. a) 1x2 switch structure. b), c) Optical field intensity for b) aGST and c) cGST [19].

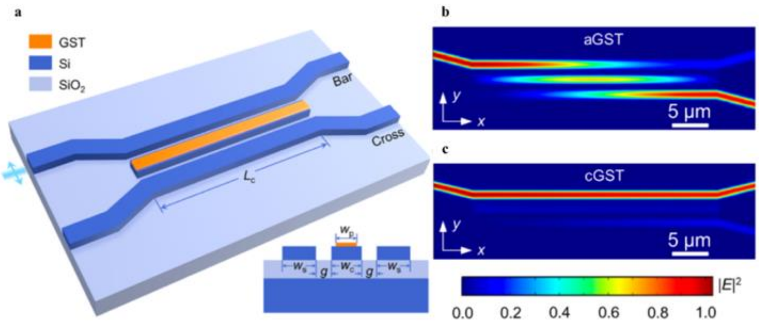

Fig. 5. a) 2x2 switch structure. b), c) Optical field intensity for b) aGST and c) cGST [19].

Interestingly, similar results are found in [15]. On account of its significant lower attenuation, identical structures are simulated using GSST instead of GST. Table 3 shows a comparison in terms of insertion losses and crosstalk. As evident, the use of GSST implies a significant improvement.

	GST	**GSST**
Insertion Losses (dB)	8.6	3.5
Crosstalk (dB)	-0.02	-6.1

Table 3. Performance comparison of a 2x2 switch design using GST and GSST [15].

Other structures like ring resonators may also be employed. In [21] authors demonstrate an energy-efficient, compact and non-volatile all-pass ring integrated with GST. The state of the GST layer determines the ring operation. In the crystalline state, attenuation is so high that almost no power will be coupled to the ring and it will all exit through the straight waveguide. The ring is designed in such way that, in the amorphous state, critical coupling is achieved and there is no power at the output. A very recent work [20] also exploits GST by integrating it with an add-drop (2x2) ring resonator. The GST pattern technique is particularly innovative: disks with 500 nm diameter instead of the common rectangular patches are deposited. These disks can be more uniformly heated than a patch with a relatively wide area.

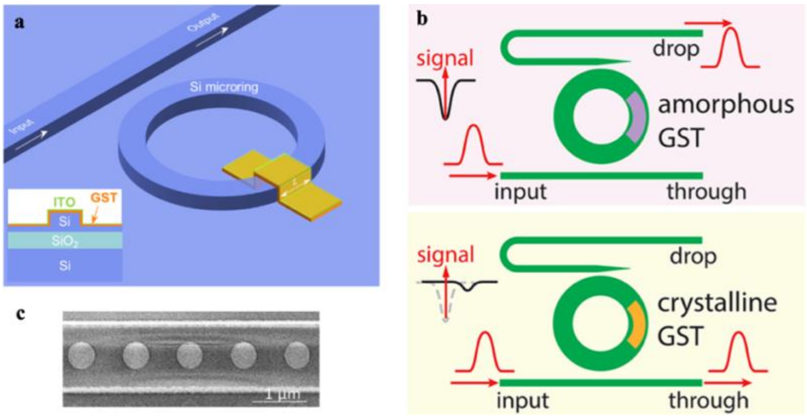

Fig. 6. **a)** Schematic of the all-pass ring demonstrated in [21]. Inset: cross-section of the hybrid waveguide. **b)** Operation description of the add-drop ring and **c)** GST pattern [20].

Optical memories

The architecture of modern computers follows the model developed by John von Neumann in 1945. Computers consist of a Central Processing Unit (CPU) containing a Control Unit and an Arithmetic/Logic Unit, memory and input/output (I/O) components. Programs and data are stored in memory, a storage unit separated from the processor. As information flows between these two components, latency is inevitable. In recent years, processors' computing capabilities and speeds have increased considerably, while memory developments have mostly been in the line of density rather than transfer rates. Super-fast processors need to wait for data to be fetched from memory; this limitation of the throughput is also known as the "von-Neumann bottleneck". In addition, if an optical link between electronic memory and processor is considered, a signal transformation between domains is needed. This would result in excessive time and power consumption. This scheme may not be suitable for some applications. Therefore, a fully integrated optical memory may be valuable [22].

Phase-Change Materials are excellent candidates due to their self-holding feature, thermal stability, high index change and fast transition between states. The first successful application of PCMs was in rewritable optical data storage. A voltage pulse was used to change the state of the PCM confined in a cell. The writing process was performed by transitioning the cell to the amorphous state. When transitioning back to the crystalline state, recorded information was erased [10].

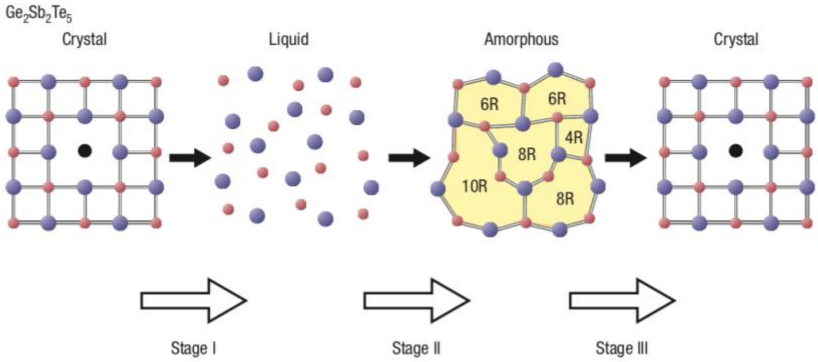

Fig. 7. Stage I and II represent the recording process, stage III represents the erasing process in optical storage using GST [10].

Cell sizes of 7.5 nm x 17.5 nm have been realized [11], demonstrating the integration potential. Switching times in the nanosecond range were achieved, suggesting that PCMs could be used to build a memory possessing the best properties of flash and DRAM memories.

In [13], the authors explore the prospect of an all-photonic non-volatile memory with multi-level operation capability using GST. The memory cell consists of a waveguide with a GST layer on top. Reading and writing of the cell is performed through evanescent coupling between the light travelling through the waveguide and the GST layer. When

GST is in the crystalline state, it shows a very high attenuation. If we introduce an optical pulse through the waveguide, the GST layer on top will pull the light towards it, resulting into a very attenuated optical signal at the output. On the other hand, in the amorphous state, the waveguide transmission is not that highly attenuated and the light will travel through. Therefore, the content of the memory cell is encoded in the state of the GST layer (i.e. '0' in crystalline state, '1' in amorphous). For the writing process, a higher energy pulse with a different wavelength capable of triggering the state switch is used. By carefully controlling this pulse, intermediate states were achieved, allowing for multi-level operation. Fig. 8 shows a schematic of the described memory cell.

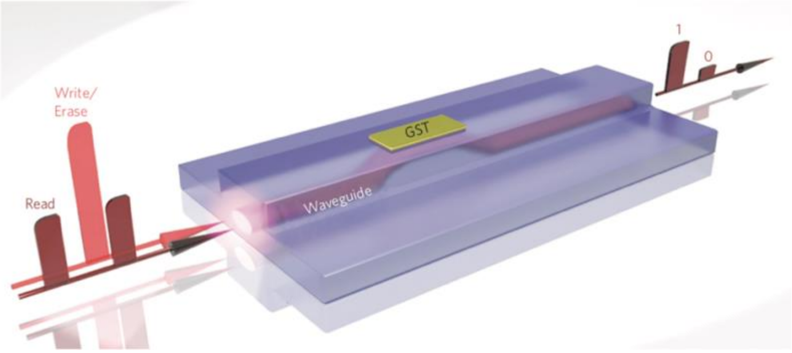

Fig. 8. Memory cell structure. Reading and writing is done with short optical pulses. Information is encoded in the optical power at the output when a reading pulse is applied [10].

Optical Modulation

An optical modulator is a device that modulates (i.e. varies specific characteristics, such as amplitude, phase or polarization) a beam of light. Some figures of merit used to evaluate the performance of an optical modulator are the modulation speed, modulation depth (or extinction ratio), bandwidth, insertion losses, energy consumption (defined as energy per produced bit) and footprint. A trade-off among them needs to be achieved. The ideal modulators would show high modulation speeds, large bandwidths, small footprints, low losses and low power consumption [23].

The most common methods to perform modulations in silicon are based on the change in the refractive index by leveraging the electro-optic effect (applying an electrical voltage) or the thermo-optic effect (regulating the temperature). As a result of the limited tunability of silicon's optical properties, two main methods are followed to transform the index contrast into a power modulation. Firstly, by controlling the shift of signals in a Mach-Zehnder interferometer such that they interfere constructively or destructively at the output. Secondly, employing a resonant structure in which the index change varies the resonant wavelength. The first method usually results in devices requiring larger lengths, which makes them harder to be integrated, while the latter leads to devices which are very sensitive to temperature drifts and show narrower bandwidths. The integration of silicon waveguides with active materials such as Phase-Change Materials that offer a superior optical tunability is proposed as a solution.

Phase-Change modulation schemes can usually be categorized into two groups: phase modulations, that leverage the change in the real part of the refractive index, and loss modulations, that make use of the change in the imaginary part. In [14], the authors show an example of the latter by electrically inducing the phase transition in GST using a layer of copper on top. As seen in Fig. 9 b), when GST is in the amorphous state, the power is mainly confined in the middle of the waveguide. When GST is triggered to the crystalline state, power confinement in the active layer is dramatically enlarged. A light wave travelling through the waveguide will suffer more or less attenuation depending on the state of GST. Therefore, the modulation of the applied voltage effectively modulates the output power. The demonstrated device has an ultra-small footprint (0.2 μm^2), large modulation depth (11 dB/μm) and low energy consumption (357 pJ/cycle).

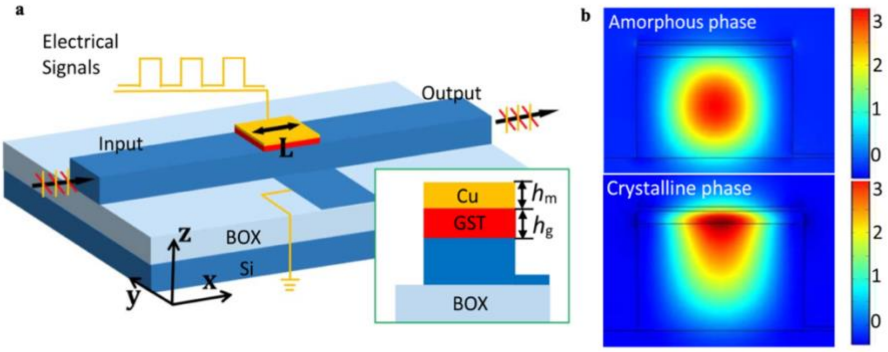

Fig. 9. **a)** Proposed hybrid Si-GST-Cu waveguide. **b)** Mode profiles in amorphous and crystalline state [14].

In [24] and [25], VO_2 instead of GST is employed as the active material. This causes the applications to be volatile. Nevertheless, we briefly present some results here because of the extensive use of VO_2 in modulators. The authors in [24] demonstrate an absorption modulator based on an all-pass ring resonator, showing modulation depths higher than 6.5 dB and 2 dB of insertion losses on a 2 μm active length. By controlling the temperature of the sample, VO_2 is switched between states. The difference in refractive index will induce a shift in the ring's response. This will allow to work at a given resonant wavelength in one state and away from it in the other. In [25], VO_2 is embedded in a Si ridge waveguide on SiO_2 substrate instead of placing a layer on top of it, which is the typical configuration. The authors demonstrate that this geometry provides a larger modulation depth as a result of the enhanced interaction of the guided mode with VO_2. The material is also transitioned by controlling the temperature. Input light wave is highly attenuated in the metallic state and is detected at the output in the semiconducting one. The resulting modulator shows a modulation depth and insertion losses of 13.8 dB and 2.2 dB, respectively. The use of a granular VO_2 layer on top of Si waveguides has also been demonstrated to minimize insertion losses [26].

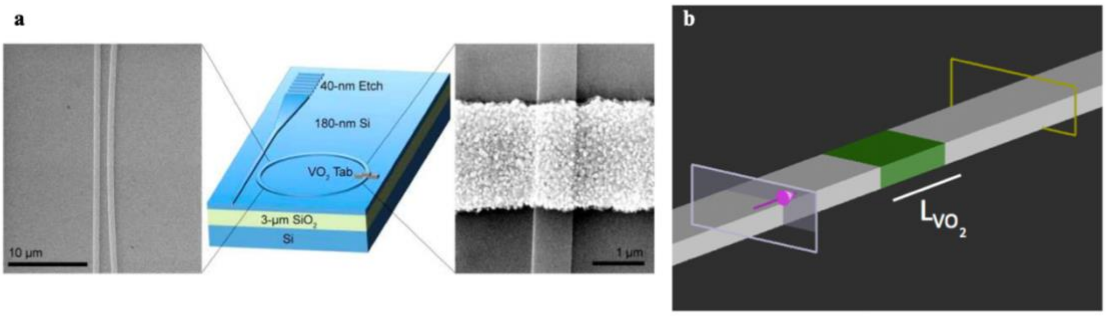

Fig. 10. **a)** Schematic of the ring modulator showing scanning electron microscopy (SEM) images of the waveguide (left) and the VO_2 layer (right) [24]. **b)** Proposed structure in [25], VO_2 integrated within the waveguide.

Neuromorphic computing

Neuromorphic computing is a term coined by Carver Mead in the late 1980s that describes the use of computers/systems that model the biological architectures present in the brain. The two main functional units in the brain are the neurons and the synapses. A neuron is an electrically excitable cell that processes and transmits information. When a signal reaches the end of a neuron, it does not directly get transferred to the next one. Instead, it encounters a synapse: a gap where neurotransmitters are triggered. These neurotransmitters are able to excite the next neuron, so the impulse is propagated. The so-called “synaptic weight” refers to the “connection strength” between neurons. Neural networks are computing systems that try to emulate the behaviour of neurons and synapses in the brain.

Original neural networks were implemented using software solutions. Despite the powerful algorithms that were developed, the software-based approaches could not deal with large-scale tasks like image and pattern recognition. Notably, they also required a significant amount of energy more than the human brain [27]. This is why new hardware architectures that could mimic both structure and function of the brain attracted research interest. Nevertheless, traditional computer architectures are limited by the already-mentioned von-Neumann bottleneck: information needs to travel back and forth between processor and memory, resulting in latencies. Computing units where memory and processing are integrated are needed in order to implement brain-inspired systems. Fig. 11 exemplifies the so-called “in-memory computing”. In Fig. 11 a), if *f(A)* is to be computed, *A* needs to be fetched from memory. In Fig. 11 b) however, *A* is already located where *f(A)* is performed, saving energy and time [28].

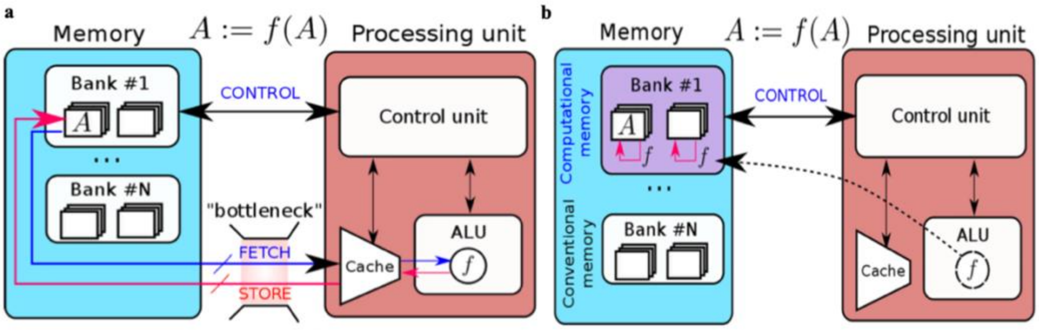

Fig. 11. **a)** Traditional computing architecture vs. **b)** in-memory computing [28].

The typical structure of a neural network or artificial neural network (ANN) is depicted in Fig. 12. In every layer, information gets transformed by a linear operation (like matrix multiplications) and a non-linear function. The input layer receives information from the outside world. Hidden layers transform inputs into useful data for the output layers. Output layers elaborate an appropriate response. Connections between layers have a weight, defining the amount of influence that one unit has on another (analogous to the synapse weight). As the information flows through the layers, the network learns more about it.

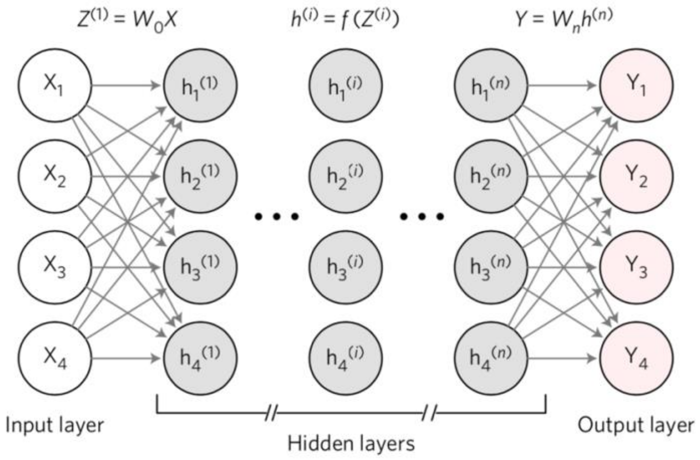

Fig. 12. Architecture of a typical ANN [29].

ANNs have a series of characteristics that make photonic circuits best suited to meet them:

1. ANNs mainly perform matrix multiplications. Photonic networks can execute linear transformations at rates exceeding 100 GHz. Processes like matrix operations or the Fourier Transform can be quickly completed.
2. ANNs perform non-linear operations that can be carried out by inherent optical nonlinearities.

3. After the network has been trained, no additional energy is required because the network starts working passively.

The integration of Phase-Change Materials is expected to play a key role in the development of brain-inspired computing using photonics. Their most attractive property is the ability to vary the optical absorption level in a controllable way, reaching intermediate levels of atomic organization. PCM-based devices have already been demonstrated. In [30], the employment of several thinner GST patches on top of a Si waveguide enables the emulation of the operation of a synapse. In [28] and [31], the authors exemplify the use of Phase-Change memory units in a neural network by exploiting the variation of conductance/resistance and how they would perform matrix multiplications.

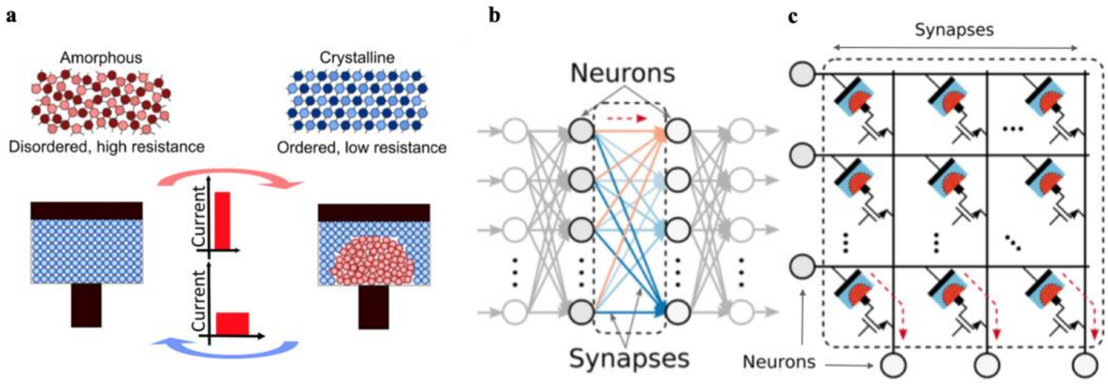

Fig. 13. **a)** Memory unit employing a PCM and detail of phase transition [28]. **b)**, **c)** Schematic of the application of PCM-based devices as synaptic units in a neural network [31].

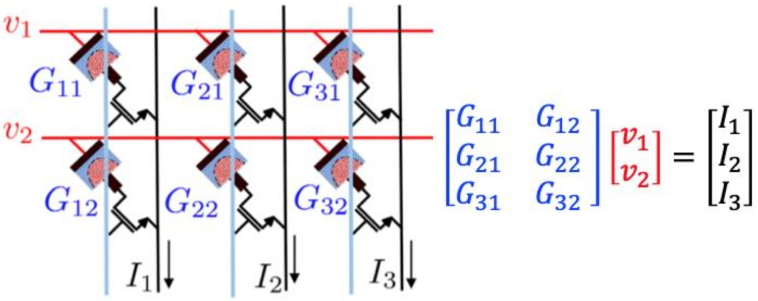

Fig. 14. Matrix multiplication (*Gv*=*I*) can be carried out by linearly mapping the values of *G* to the conductance levels of PCM devices organized in a cross-bar configuration [28].

The integration of PCM in photonics for neuromorphic computing would ultimately allow the realization of large-scale photonic neuromorphic networks similar to state-of-the-art electronic neuromorphic computers but operating at powers approaching that of the human brain [30].

2. Objectives and methodology

2.1. Objectives

The **main objective** of this work is to develop novel photonic devices based on the integration of active materials with a non-volatile optical response in the silicon photonics platform. In particular, the employment of GST will be examined, which may allow to implement high performance ultra-compact devices due to its unique properties.

For this purpose, the following **specific objectives** need to be addressed:

- Design and analysis of a hybrid GST/Si waveguide with low losses.
- Design and analysis of a ring resonator optical switch based on the developed hybrid GST/Si waveguide.
- Design and analysis of a Mach-Zehnder interferometer optical switch based on the developed hybrid GST/Si waveguide.
- Characterization of experimental samples and validation of designs.
- Discussion of the obtained results and proposal of optimized hybrid GST/Si based photonic devices.

2.2. Methodology

In order to fulfil the above mentioned objectives, the methodology followed in this research work is laid out in three main blocks: (1) documentation and state-of-the-art review, (2) device design and (3) experimental characterization, interrelated as seen in Fig. **15**. This work has been carried out at Nanophotonics Technology Center (NTC) and supervised by Prof. Pablo Sanchis Kilders, head of the Optical Modulators NTC research line.

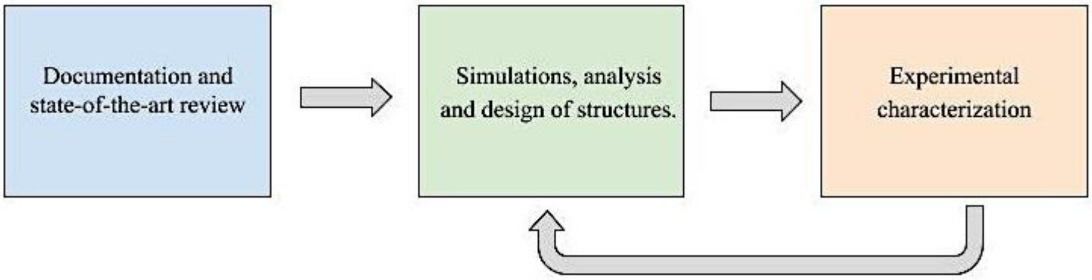

Fig. 15. The three essential blocks in the methodology and their relationship.

Each block at the same time is subdivided in:

- Block 1: documentation and state-of-the-art review.
    - Learning of photonics and integrated photonics fundamentals.
    - Reading of related scientific articles.
    - Review of the state of the art.
- Block 2: design of hybrid GST/Si photonic devices.
    - Development of MATLAB code to simulate, analyze and design ring resonator and Mach-Zehnder interferometer structures.
    - Definition of specifications and design of hybrid GST/Si photonics devices with non-volatile switching performance.
- Block 3: experimental characterization
    - Passive measurements.
    - Thermo-optic measurements.
    - Discussion and analysis of obtained results.

The two main software programs employed are FemSIM and MATLAB. FemSIM is a generalized mode solver based on the Finite Element Method (FEM) integrated in the RSoft CAD Environment and was used to carry out the design of the waveguide. The modelling and analysis of the ring and Mach-Zehnder interferometer structures was performed in MATLAB.

Fig. 16 shows a temporal chart of the distribution of tasks, starting in February 2019 and finishing in June 2019.

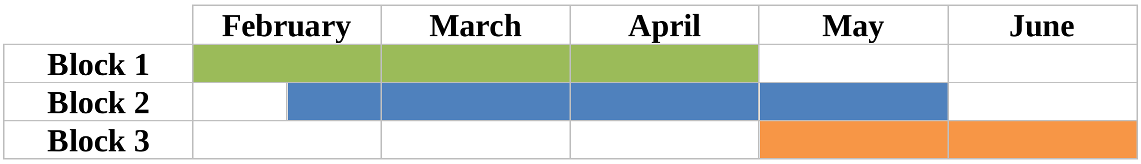

	February	**March**	**April**	**May**	**June**
Block 1	🟩	🟩	🟩		
Block 2	⬜🟦	🟦	🟦	🟦	
Block 3				🟧	🟧

Fig. 16. Diagram showing temporal distribution of tasks.

3. Non-volatile optical response component design

3.1. Description of parameters of selected materials

The active material to be used for the components' design is **GST** integrated with silicon waveguides. The first step is to obtain its optical constants. Table 4 gathers the values of refractive index of GST in both states used in four different articles, specifying whether it is a simulation-based or experimental paper, and the thickness of the GST layer used. It is important to note that properties of GST depend strongly upon the details of fabrication [25].

Ref.	n (aGST)	n (cGST)	Simulation/ Experimental	GST thickness
[32]	4.03654+0.03746i	6.49615+1.0655i	Simulation	15-25nm
[33]	3.9027+0.0055i	6.0769+0.9040i	Experimental (RF sputtering)	20nm
[22]	3.94+0.045i	6.11+0.83i	Experimental (Sputtering)	10nm
[25]	4.60+0.12i	7.45+1.49i	Simulation	10nm

Table 4. Literature review of GST parameters.

References [33] and [22] are experimental papers, therefore the derived indices are considered to be more reliable than simulation-based ones. Both papers document very similar values except for the extinction coefficient in the amorphous state. A comparison between these two references is carried out in order to analyze the influence of the refractive index of GST on our design.

3.2. Design and analysis of the hybrid waveguide

The first step is to design and analyze the hybrid waveguide to be used in the optical structures. The proposed geometry consists in a SiO_2 substrate (*n*=1.44468) and a Si waveguide (*n*=3.481) with width *W*=500nm and height *H*=220nm, on top of which GST layer is deposited. These dimensions are standard in silicon photonics circuits.

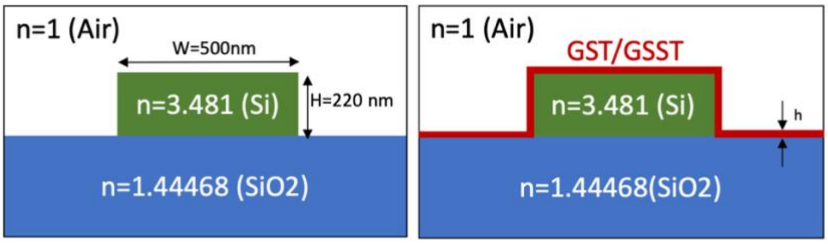

Fig. 17. Proposed geometry for the hybrid waveguide.

In this section, a modal analysis of the structures using FemSIM [34] is performed. This is done to later derive the effective refractive indices and the mode absorption loss (α [dB/µm]) from the following formula:

$$\alpha = 4.343\,\frac{4\pi k}{\lambda} \tag{2}$$

The goal is to find the optimal GST thickness *h* that will lead into an appropriate level of attenuation and active length for our design. We evaluate the effect of using the values of GST refractive indices in [33] and [22] separately.

In [33], as stated in Table 4, $\boldsymbol{n_{aGST}=3.9027+0.0055i}$ and $\boldsymbol{n_{cGST}=6.0769+0.9040i}$. Mode profile simulations result in:

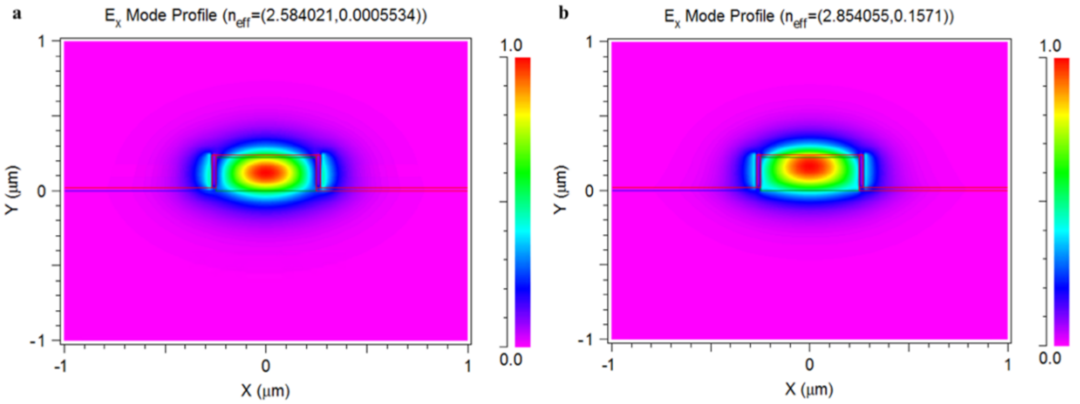

Fig. 18. Mode profiles using refractive index values from ref. [33]**,** for a GST layer thickness *h* of 20nm. **a)** Amorphous GST, **b)** Crystalline GST**.**

In [22], $\boldsymbol{n_{aGST}=3.94+0.045i}$ and $\boldsymbol{n_{cGST}=6.11+0.83i}$. There is a significant increase in the extinction coefficient *k* in aGST (of one order of magnitude).

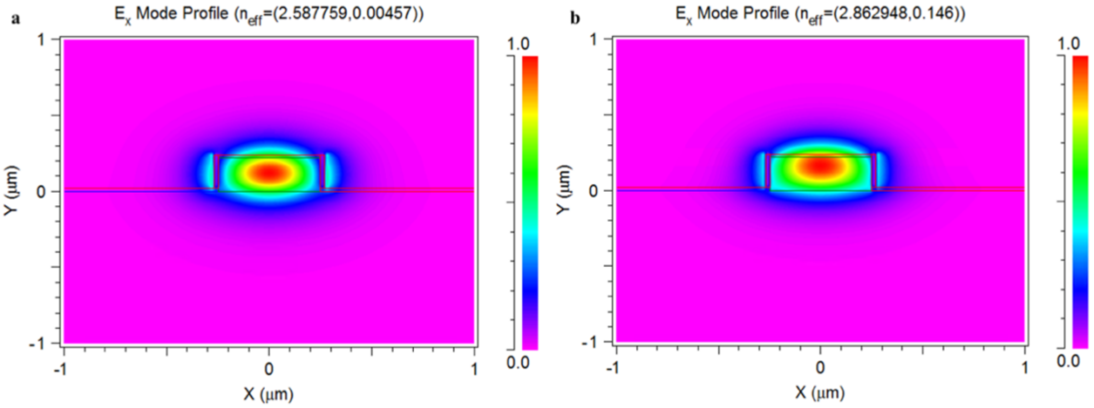

Fig. 19. Mode profiles using refractive index values from ref. [22], using a GST layer thickness *h* of 20nm. **a)** Amorphous GST, **b)** Crystalline GST**.**

The field profiles in both cases show that, when GST is in the amorphous state, the mode is confined in the middle of the waveguide and lightly spreads to the GST layer on top, the air and the SiO_2 substrate. On the other side, the acute increase of both real and imaginary parts of the refractive index after the transition to crystalline state “attracts” the field towards the GST layer.

In order to evaluate what the effect of h is, a parametric simulation is performed, ranging from 10 nm to 30 nm. Both extremes are feasibly manufactured. Complex effective refractive indices, mode absorption loss, phase shift and GST length as a function of h are computed.

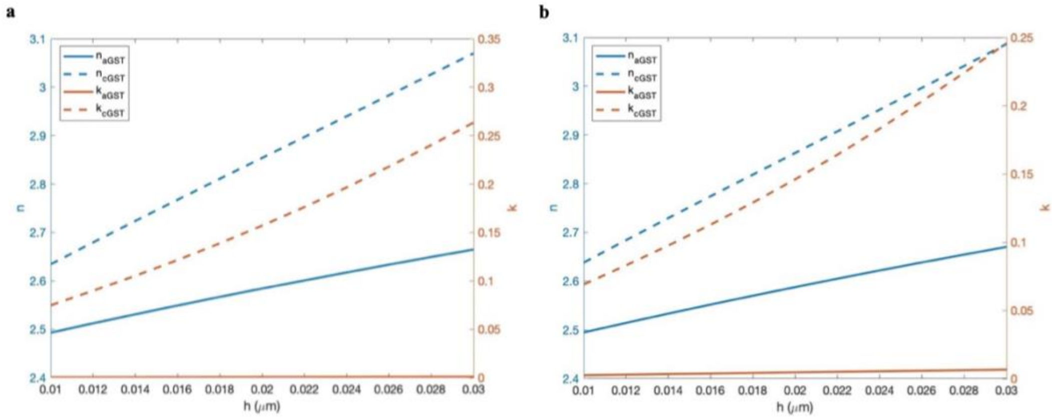

Fig. 20. Complex effective refractive indices in both states using **a)** ref. [33] and **b)** ref. [22] as a function of the GST layer thickness h.

The values of the complex effective refractive index on the structure in both cases are similar, except for the extinction coefficient k in the amorphous state. This difference leads to different mode absorption (Fig. 21). α [dB/µm] is calculated using Equation (2). In crystalline state, both references generate similar values of attenuation, but in amorphous state there is a considerable difference.

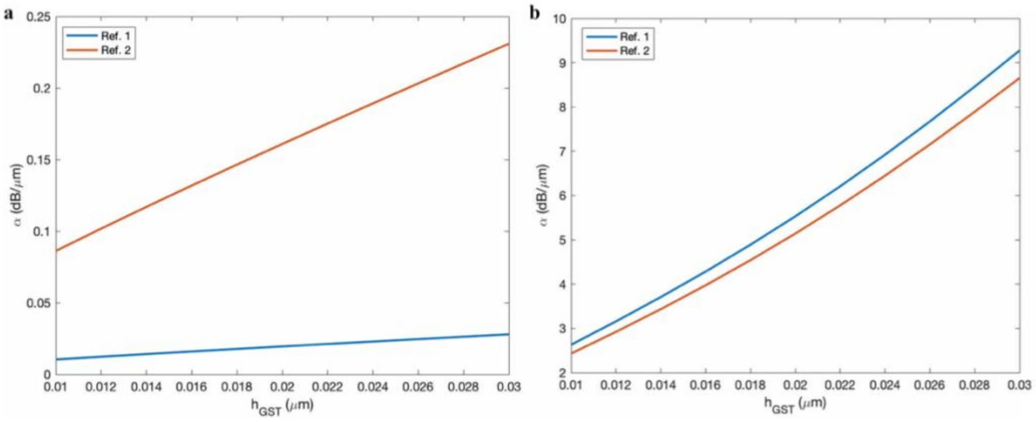

Fig. 21. Mode absorption loss (dB/µm) as a function of h in **a)** aGST and **b)** cGST for both ref. [33] and ref. [22], represented as Ref. 1 and Ref. 2 in the figures, respectively.

Next, we found the phase shift $\Delta\emptyset$ that the state transition generates. Equation (4) derived from (3), is used for this purpose. In Δn_{eff} only the change in n (real part) is considered. Fig. 22 presents the results, showing very similar values.

$$\Delta\emptyset = \Delta n_{eff}\,\frac{2\pi}{\lambda}L \tag{3}$$

$$\Delta\emptyset\,\left(\frac{\pi}{\mu m}\right) = \Delta n_{eff}\,\frac{2}{\lambda} \tag{4}$$

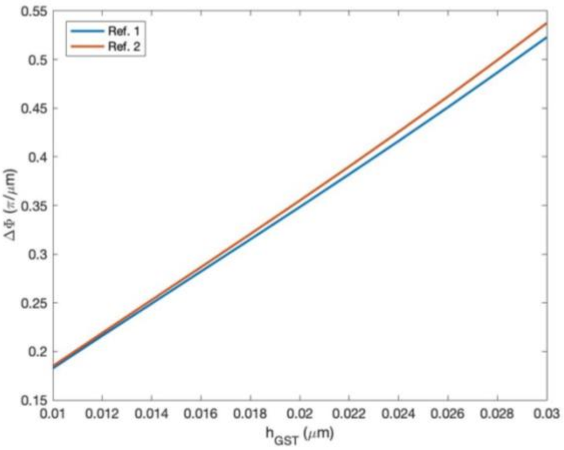

Fig. 22. Phase shift per μm as a function of *h*.

In order for GST to be suitable to develop optical switches (i.e. the building block of photonic integrated circuits), a phase shift of π must be achieved between state transitions. Details about this requirement are explained in following sections. Fig. **23** depicts the length of the GST layer that allows the accomplishment of this condition. Again, very similar values are observed.

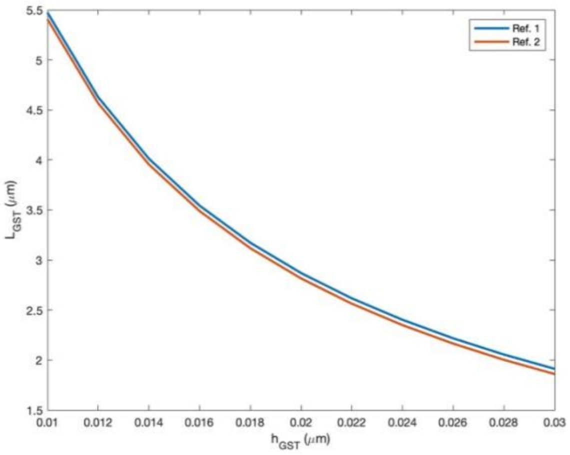

Fig. 23. Length of the GST layer that results in a phase shift of π.

The total absorption loss when the calculated values of GST length are used is presented in Fig. 24.

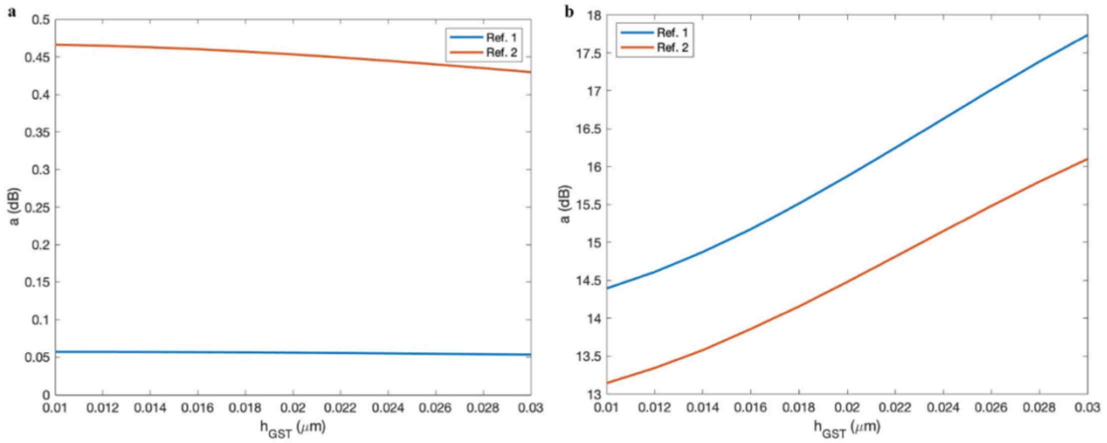

Fig. 24. Total losses in **a)** aGST and **b)** cGST for both references.

In the amorphous state, [33] results in losses 9 times lower than ref. [22], while in crystalline they appear to be 2 dB higher. Considering L_{GST} is minimized for higher values of h but losses are minimized in the opposite case, the chosen GST thickness is ***h*=20nm**, which is a typical and feasibly manufactured value. Table 5 gathers the GST length and total losses for both references if this thickness was used.

	Ref. [33]	**Ref.** [22]
GST Length (μm)	2.8700	2.8162
Total losses aGST (dB)	0.0559	0.4531
Total losses cGST (dB)	15.8732	14.4801

Table 5. Comparison of L_{GST} and losses for both references.

Seeing that L_{GST} and losses in crystalline state are nearly the same but losses in amorphous using ref. [33] are considerably lower, we decide to use it as a reference for the values of refractive index of GST. This allows us to achieve the best switching performance.

3.3. Design and analysis of a ring resonator-based optical switch

Theoretical framework

Ring resonators are one of the most common structures in integrated photonics. The most basic ring (all-pass ring) consists in a looped waveguide with a circular or racetrack shape, and an adjacent straight waveguide. Optical power travelling through the straight waveguide is coupled to the ring. A resonance will occur if the length of the ring is an integer number of the signal's wavelength, therefore resulting in a constructive interference. Multiple resonances are supported. Spacing ($\Delta\lambda$) between them is known as *Free Spectral Range* (FSR). Common applications of ring resonators are optical filters, delay lines or dispersion compensators and modulators/switches.

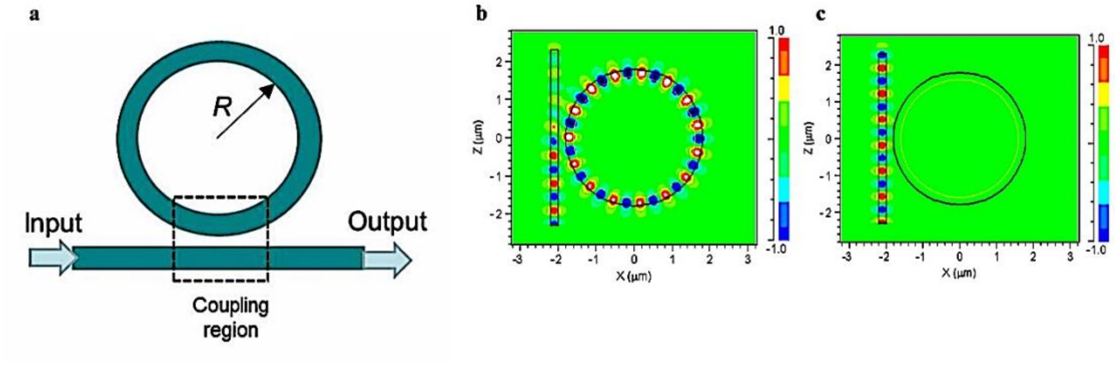

Fig. 25. **a)** Structure of an all-pass ring. **b)** Resonant mode. **c)** Non resonant mode.

Another typical configuration is the so-called "Add-Drop" ring resonator, shown in Fig. 26. This is the structure used for the design of our optical switch. The looped waveguide is coupled to two straight waveguides. The input field is transmitted to both Trough (also called Pass) and Drop ports. Equations (5) and (6) describe the transfer function at each port [35]. MATLAB code used to analyze the ring response is located in Appendix 1.

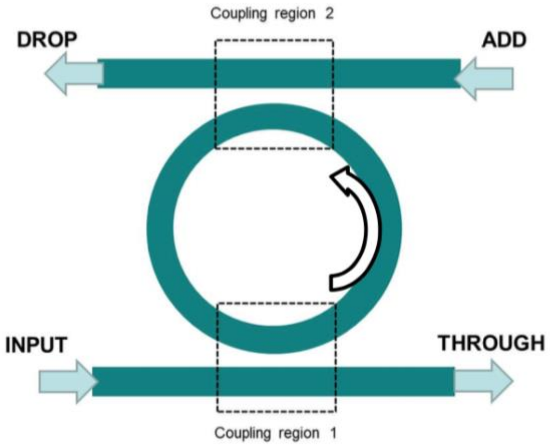

Fig. 26. Add-Drop ring resonator schematic.

$$\frac{E_{pass}}{E_{in}} = \frac{t_1 - t_2^* \sqrt{A} e^{j\emptyset}}{1 - \sqrt{A} t_1^* t_2^* e^{j\emptyset}} \tag{5}$$

$$\frac{E_{drop}}{E_{in}} = \frac{-k_1^* k_2 \ A^{\frac{1}{4}} e^{j\frac{\emptyset}{2}}}{1-\sqrt{A} t_1^* t_2^* e^{j\emptyset}} \tag{6}$$

where t₁ and k₁ are the self-coupling and cross-coupling coefficients of Region 1, respectively; t₂ and k₂ are the corresponding of Region 2. The four are derived from the coupling coefficients K_1 and K_2, that represent how much optical input power is coupled to the ring, ranging from 0 (no coupled power) to 1 (all input power is coupled). The coupling coefficients depend on the coupling length (L_c) and the distance between the ring and the straight waveguides (d). The exact value of the coupling coefficients is computed using Finite-Difference Time-Domain (FDTD) simulations. Coupling regions are assumed to be lossless, therefore:

$$t^2 + k^2 = 1 \tag{7}$$

$\emptyset = \beta L$ is the phase shift, with β being the propagation constant of the guided mode and L the length of the ring. Resonant modes occur at $\emptyset = 0, 2\pi, 4\pi \ldots$ Finally, A represents the losses. Table 6 gathers the expressions of these parameters.

Parameter	Expression	Eq. Ref.
$\boldsymbol{t}$	$\sqrt{1-K}$	(8)
$\boldsymbol{k}$	$\sqrt{K}$	(9)
$\emptyset$	βL	(10)
$\boldsymbol{\beta}$	$n_{eff}\frac{2\pi}{\lambda}$	(11)
$\boldsymbol{A}$	$e^{-\alpha L}$, with α [Np/m]	(12)

Table 6. Parameters needed for the ring resonator design.

Other important expressions to be considered are: *Free Spectral Range* (FSR), which is the spectral distance between two resonances and the *Full Width at Half Maximum* (FWHM), that represents the 3-dB bandwidth of the resonant wavelength. From the spectral response of the ring, another two relevant measurements are the *Extinction Ratio* (ER), that in this context can also be called *Crosstalk* (CT), and the *Insertion Losses* (IL) (Fig. 27).

$$\text{FSR} = \frac{\lambda^2}{n_g L} \tag{13}$$

$$\text{FWHM}= \frac{\left(1-t_1t_2\sqrt{A}\right)\lambda^2}{\pi n_g L\sqrt{t_1t_2\sqrt{A}}} \tag{14}$$

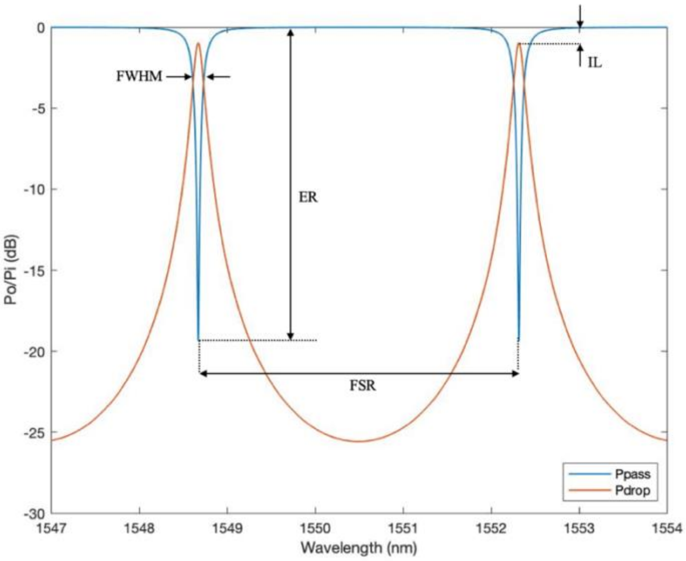

Fig. 27. Typical response of an add-drop ring resonator.

It is important to note the difference between n_g (group index) and n_{eff} (effective index). The group index takes into account the dispersion of the waveguide.

$$n_g = n_{eff} - \lambda_{res}\frac{dn_{eff}}{d\lambda} \tag{15}$$

It is therefore necessary to calculate the effective refractive index as a function of the wavelength for the waveguide with and without GST. For this purpose, a parametric analysis using FemSIM is carried out. The expression of n_{eff} (λ) can be modelled as a first-degree polynomial (Eq. (16)), with C as a constant to be determined. The expressions are obtained using the integrated MOST simulation tool of FemSIM and derived with MATLAB.

$$n_{eff}(\lambda) = C\lambda + n_g \tag{16}$$

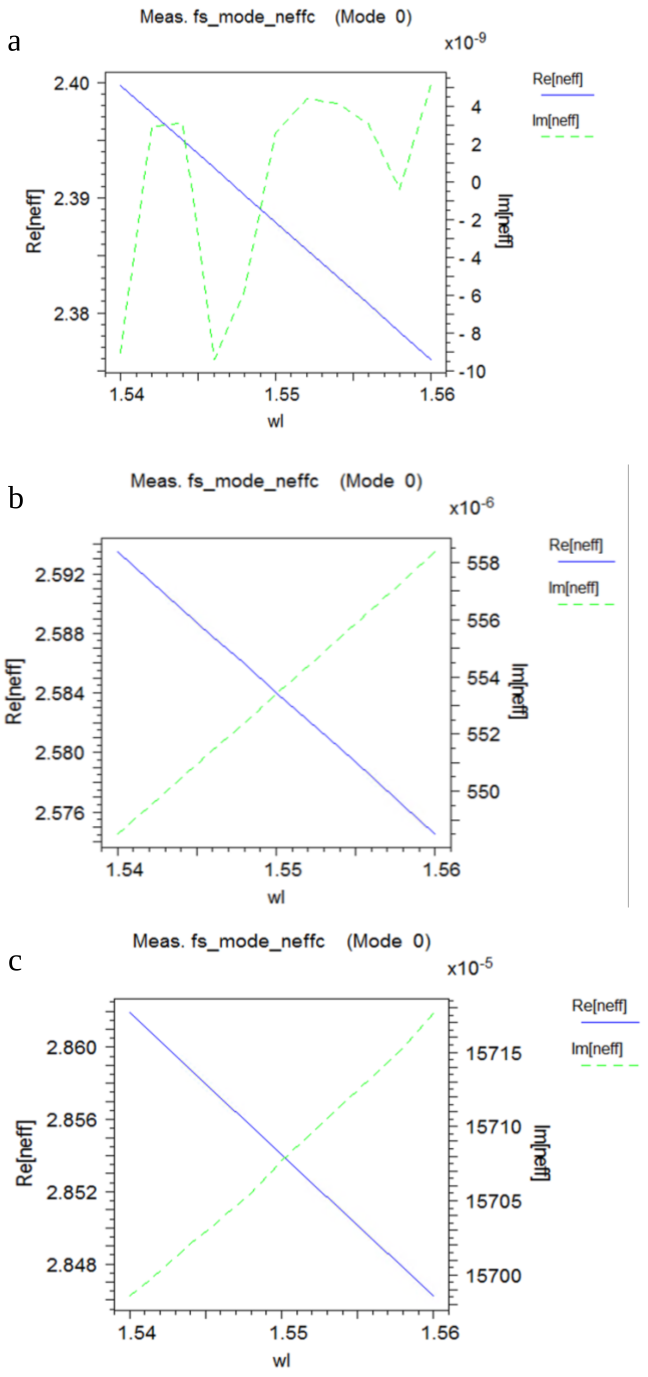

$$n_{eff}(\lambda) = -1.1850\lambda + 4.2246 \tag{17}$$

$$n_{eff}(\lambda) = -0.9442\lambda + 4.0475 \tag{18}$$

$$n_{eff}(\lambda) = -0.7839\lambda + 4.0692 \tag{19}$$

Fig. 28. Effective refractive index as a function of the wavelength for **a)** the waveguide without GST and the waveguide with the GST layer in **b)** amorphous and **c)** crystalline states. Wavelength units are in micrometers.

The change of the effective refractive index when GST transitions between states results in a change of the phase shift the optical signal suffers on its trip along the ring. A typical response as a function of the phase shift is shown in Fig. 29. It has been represented in linear units for clarity purposes.

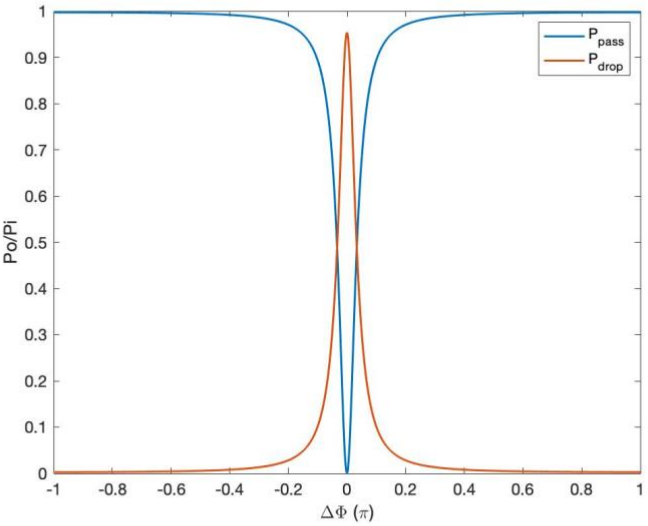

Fig. 29. Response of a ring resonator in linear units as a function of the phase shift.

A phase shift of ±π results in the power completely drifting from one port to another. This is the expected behavior of a phase-based switch. The following section provides an analysis of whether GST can induce this change and thus be considered suitable for the switch implementation.

Ring Design and Analysis

The structure to be analyzed and optimized is displayed in Fig. 30. This configuration has been chosen because of the availability of already manufactured silicon samples with these dimensions. This allows to carry out an experimental verification of the suitability of the structure for the placement of GST. Specifically, it is a racetrack ring resonator with a total length of L=42 µm and bend radius of 3.5 µm. Symmetric in both coupling regions. The losses of Si are considered to be α_{Si}=10 dB/cm. Losses of the waveguide with the GST layer are derived from Fig. 21 a), being α_{aGST}=0.0195 dB/µm and α_{cGST}=5.5307 dB/µm.

As computed in Section 3.1, the required length of the GST layer is L_{GST}=2.87 µm. This length will be divided into two sections, each of them placed on top of the 2 µm straight waveguides as seen in Fig. 30.

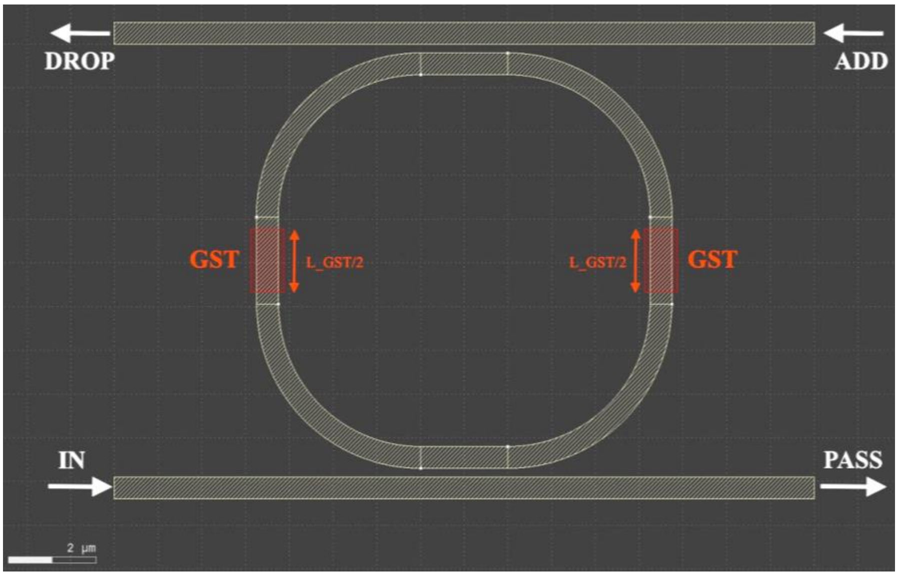

Fig. 30. Ring resonator schematic.

An initial simulation is carried out considering $K_1=K_2=0.1$ in order to locate some resonances. The resonant wavelengths within the simulated range (1542-1575 nm) are 1550.900 nm and 1564.615 nm, resulting in an FSR of 13.715 nm. A similar result is obtained if equation (13) is used: considering the group index of silicon, FSR gives 13.56 nm. As observed in Fig. 31, in the amorphous state, most of the power exits the ring through the Drop port, with a high attenuation at the Pass port. In crystalline state the operation is the opposite: all the power is located at the Pass port.

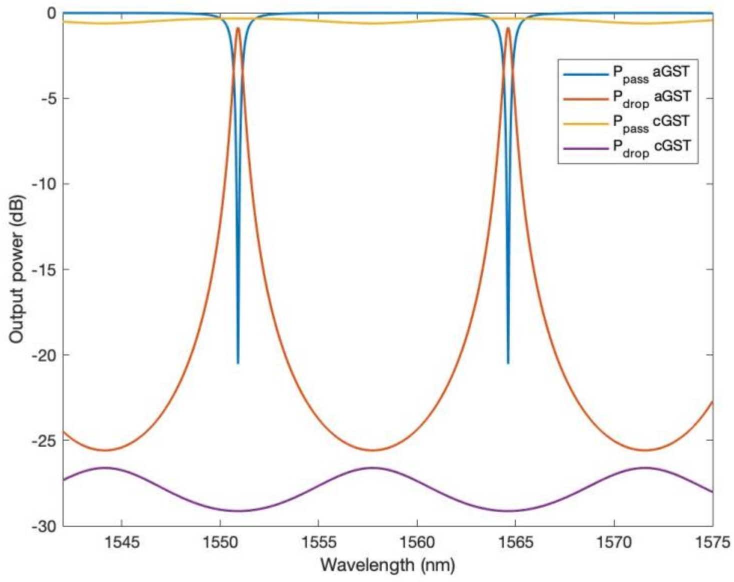

Fig. 31. Initial simulation of the designed ring.

In this section, the values of the coupling coefficients are optimized in order to obtain crosstalk values over 15 dB and insertion losses under 1 dB. These are challenging but feasible values found in the literature. Considering the application of the ring is an optical switch, symmetrical coupling is needed to have the same switching performance independently of the input port. Therefore, K_1=K_2, henceforth K . This means that the coupling length L_c and the distance between the ring and the straight waveguides d need to be exactly the same in both coupling regions. Fig. 32 shows the values of CT and IL in both states as a function of K.

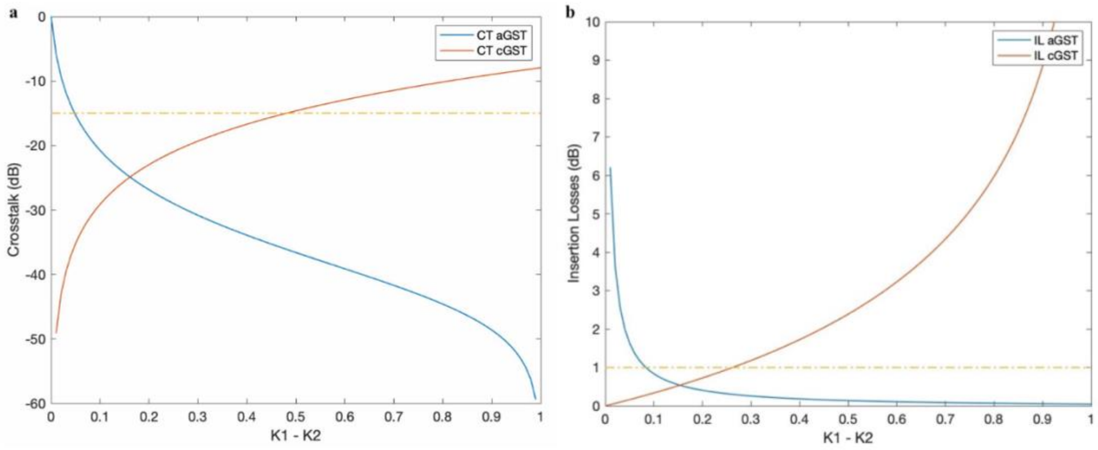

Fig. 32. Values of **a)** crosstalk and **b)** insertion losses in both states as a function of K. Horizontal lines mark the design goals: **a)** -15dB for CT and **b)** 1dB for IL.

The values of K that accomplish the crosstalk and losses conditions are **0.05-0.47** and **0.08-0.26**, respectively. Therefore, the optimal K lies in the range **0.08-0.26**. The final value is decided upon bandwidth maximization. For that purpose, Eq. (14) will be used.

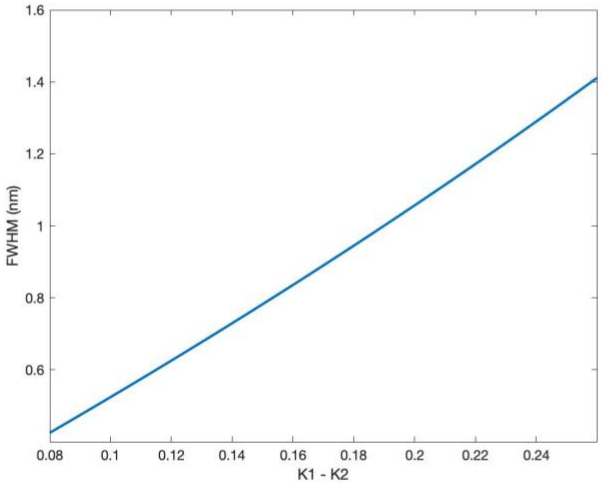

Fig. 33. FWHM as a function of K.

For ***K*=0.26**, the values of CT and IL meet the requirements and the bandwidth is maximum, with a value of 1.41 nm. This bandwidth allows data rates up to 175 GHz [36]. The response of the final design of the ring is shown in Fig. **34**.

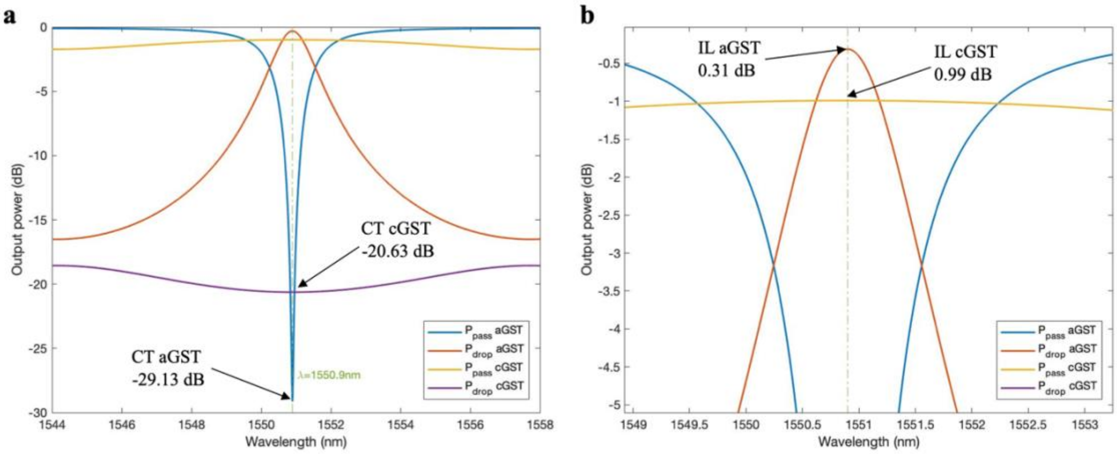

Fig. 34. Response of the designed ring centred at λ=1550.9 nm. **a)** Overview and values of crosstalk. **b)** Detail and values of insertion losses.

The following table gathers a summary of resulting parameters.

Parameter	Value
CT aGST (dB)	-29.1324
CT cGST (dB)	-20.6292
IL aGST (dB)	0.3126
IL cGST (dB)	0.9903
FWHM (nm)	1.41
FSR (nm)	13.715

Table 7. Summary of resulting parameters of the designed ring.

3.4. Design and analysis of a Mach-Zehnder interferometer-based optical switch

Theoretical framework

A Mach-Zehnder interferometer (MZI) is a photonic integrated structure widely used for modulators, especially for amplitude modulations [35]. Other applications include multiplexers/demultiplexers, optical filters and all-optical switches. It consists of a waveguide that splits into two branches by means of Y-junctions or directional couplers. Optical power is split and travels through the branches until being recombined again at the output. Depending on each branch's characteristics (i.e. length and optical properties), light signals will suffer attenuation and/or phase shifts, resulting into different kinds of interferences at the output.

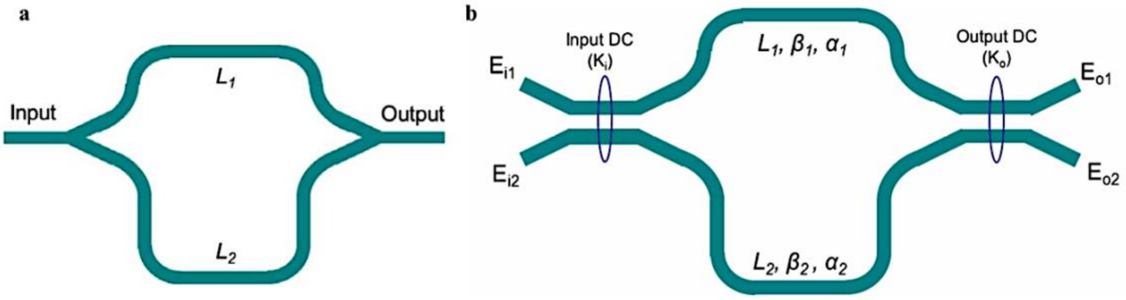

Fig. 35. **a)** 1x1 MZI using Y-junctions. **b)** 2x2 MZI using directional couplers.

In this section, a 2x2 MZI structure is used for the design of the switch. The transfer function is expressed by Eq. (20).

$$\begin{pmatrix} E_{o1} \\ E_{o2} \end{pmatrix} = \begin{pmatrix} \sqrt{1-K_o} & -j\sqrt{K_o} \\ -j\sqrt{K_o} & \sqrt{1-K_o} \end{pmatrix} \begin{pmatrix} e^{(-\alpha_1+j\beta_1)L_1} & 0 \\ 0 & e^{(-\alpha_2+j\beta_2)L_2} \end{pmatrix} \begin{pmatrix} \sqrt{1-K_i} & -j\sqrt{K_i} \\ -j\sqrt{K_i} & \sqrt{1-K_i} \end{pmatrix} \begin{pmatrix} E_{i1} \\ E_{i2} \end{pmatrix} \tag{20}$$

where K_i and K_o are the input and output coupling coefficients of the directional couplers, respectively. α_1, α_2 represent the losses in Np/m and β_1, β_2 represent the propagation constant of each branch. For this design, E_{i2} can be considered to be 0, meaning all the input power will input from port 1.

One of the most important parameters in the design of MZIs is the phase difference. The phase difference represents the deviation of phase of a signal travelling through the lower branch in comparison to the one travelling through the upper branch or viceversa.

$$\Delta\phi = \beta_2 L_2 - \beta_1 L_1 \tag{21}$$

where β_1, β_2, L_1, L_2 are the propagation constants and lengths of each branch (see Eq. (11)).

The typical response of a 2x2 MZI is shown in Fig. 36. When the phase shift is near zero ($\Delta\phi \sim 0$), the MZI is in the so-called **cross state** and all the power exits through the second port (P_{o2}). When a phase shift of π is achieved ($\Delta\phi \sim \pi$), all the power drifts to the first port (P_{o1}). This is the so-called **bar state**. GST is placed on top of both branches to have a balanced performance in the amorphous state and to induce a shift of π when the material in a given branch is switched to crystalline.

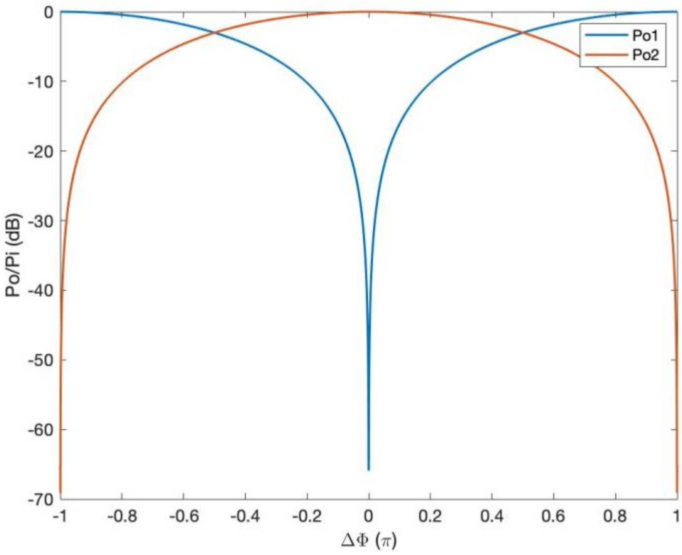

Fig. 36. Typical response of a 2x2 MZI as a function of the phase shift.

As in the ring design, losses of Si and GST and dispersion of n_{eff} with the wavelength need to be considered. Influence on ER, IL, FSR and FWHM is analyzed.

MZI Design and Analysis

The designed structure can be seen in Fig. 37. It is a symmetric 2x2 MZI of length L=10 µm. A GST layer of L_{GST}=2.87 µm will be placed on both arms. This way, the MZI is completely symmetric when both layers are in the same state and a phase shift of π is induced when one of them transitions.

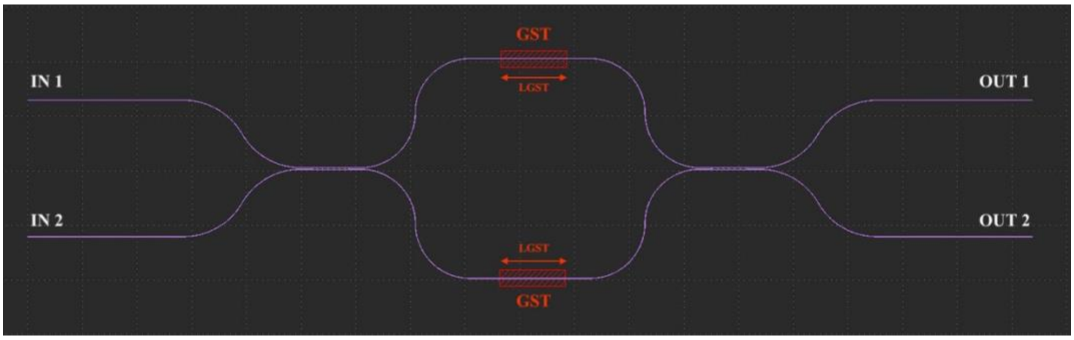

Fig. 37. Symmetric MZI with GST.

Losses and n_{eff} (λ) are taken as in the ring design. Input field is normalized to 1. Coupling coefficients are initially taken as K_i=K_o=0.5 but will be later optimized. MATLAB code used to perform these simulations is found in Appendix 1.

As explained in Section 3.4, when both branches have the exact same characteristics in terms of length and optical properties, the phase shift difference is 0 and the MZI is in the cross state: all the power will go through the second output port. When GST in the lower (or upper) branch is transitioned to the crystalline state, a phase shift of π is expected. In an ideal MZI all the power would drift to port 1. Nevertheless, losses in this state are so high that values of IL and ER are not adequate for practical applications.

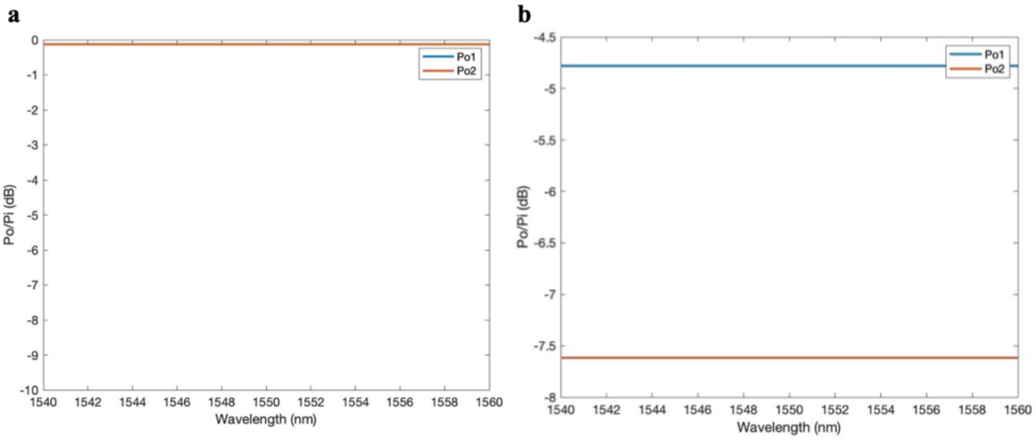

Fig. 38. Response of MZI when GST is in **a)** amorphous and **b)** crystalline states. *Po1* is not visible in **a)** because its value is -∞ (ideal).

An optimization of the value of the input coupling coefficient K_i to achieve maximal ER and minimal IL is performed. On account of the higher losses in cGST, more power is needed through the lower branch in order to balance the MZI. Therefore, the optimal value of K_i lies in the range **0.5-1**. Fig. 39 shows insertion losses and crosstalk in both states as a function of K_i. As evident, crosstalk can be minimized but only at the expense of higher insertion losses. The value of K_i that results in minimal CT in both states is $\boldsymbol{K_i=0.7455}$. Resulting response is found in Fig. 40.

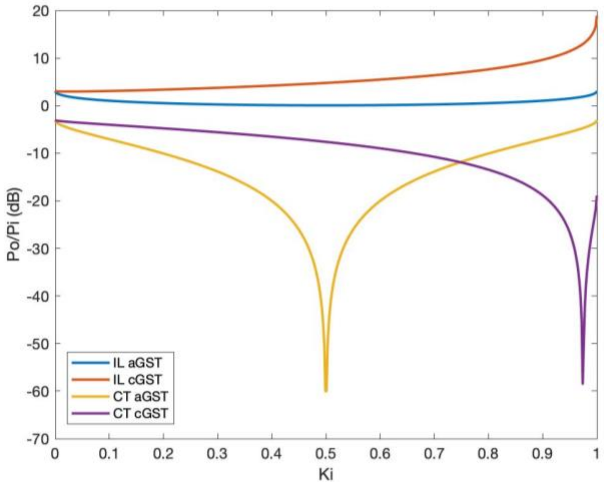

Fig. 39. IL and CT as a function of K_i in both states.

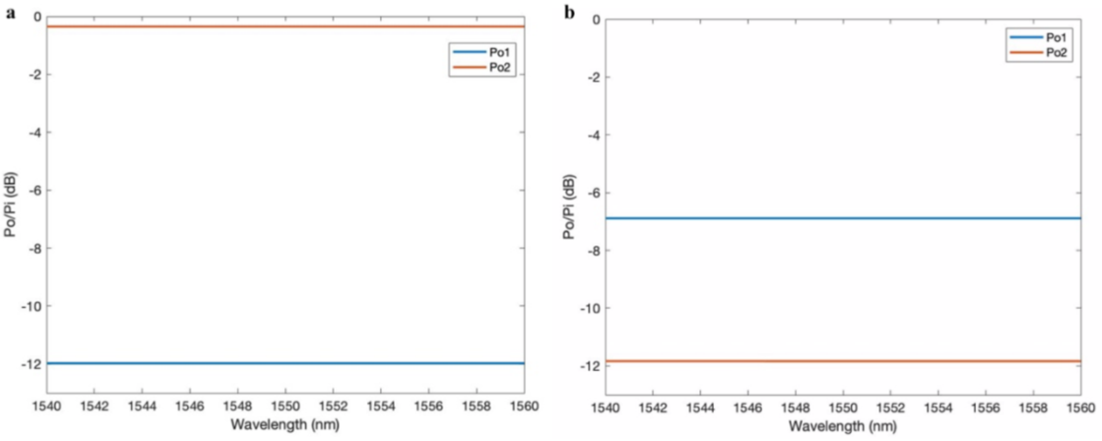

Fig. 40. MZI response for K_i=0.7455 in **a)** aGST and **b)** cGST.

The following table gathers a summary of resulting parameters. The FSR in an MZI follows formula (13) but considering *L* as the length difference between branches (ΔL). In a symmetric MZI this value is so high that, in the working region, the response is considered constant and therefore the bandwidth FWHM is significantly large.

Parameter	Value
CT aGST (dB)	-11.9729
CT cGST (dB)	-11.8341
IL aGST (dB)	0.3523
IL cGST (dB)	6.8925
FWHM (nm)	>100

Table 8. Summary of resulting parameters of the designed MZI.

It is therefore clear that an implementation of an MZI-based switch using GST would not be practical due to the high losses. The employment of GSST is proposed as a potential solution.

4. Experimental results

The purpose of this section is to analyze the passive performance of silicon-based ring resonators and the influence of temperature on their response. As described in Section 3.3, the variation of the refractive index between states of GST will result in a change of the ring's response. Considering the state transition is induced by controlling the temperature, it is important to characterize the influence of this parameter on the silicon waveguides in order to discern between effects in future implementations of devices with GST.

4.1. Description of the setup

The experimental set-up to be used to carry out the measurements is shown in Fig. **41** and Fig. **42**.

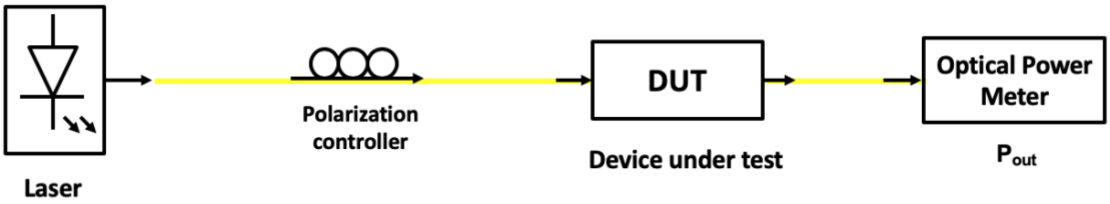

Fig. 41. Connection schematic.

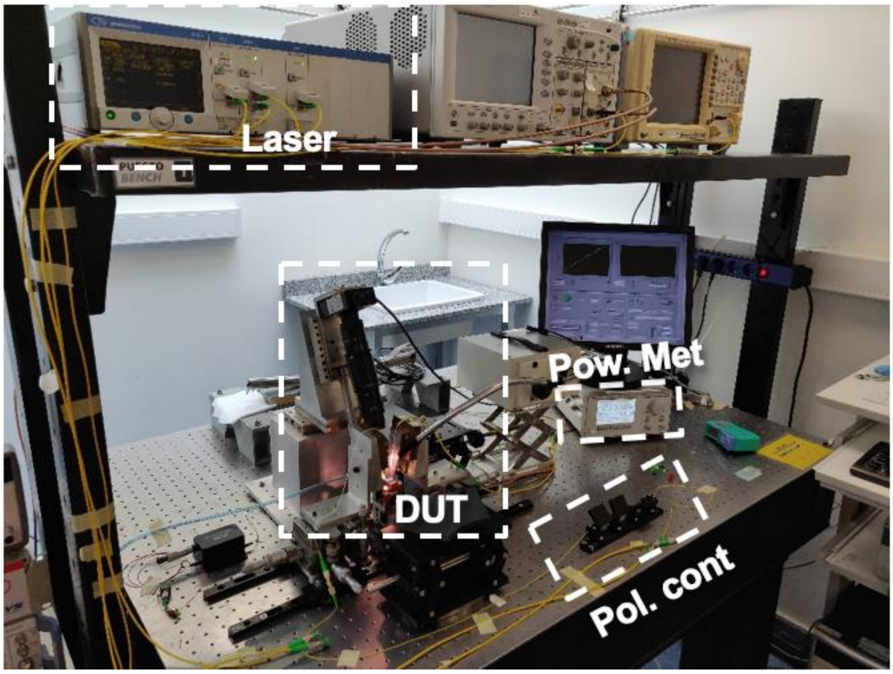

Fig. 42. Laboratory equipment to be used.

The laser is a continuous wave (CW) laser with tunable wavelength of the output signal in the range 1540-1600 nm.

The polarization controller is a device that allows to adjust the polarization of light. It consists of three fiber coils that can be rotated around an axis. The gratings where fiber optics are coupled to the integrated structures are built for a specific polarization (TE/TM). It is therefore necessary to adjust it before performing any measurement. The three paddles need to be rotated such that the maximal power is received at the output (Optical Power Meter).

The Device Under Test (DUT) or sample is located on a holder and maintained in position thanks to air suction.

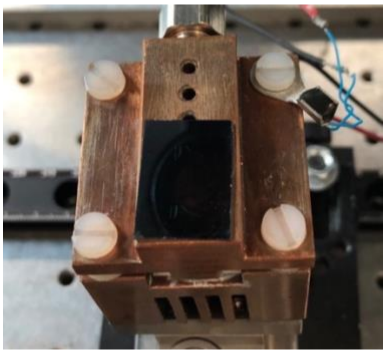

Fig. 43. Detail of the holder. The sample is maintained in position thanks to an air suction mechanism.

The input and output fiber optics are controllable in X, Y and Z by adjusting two 3-axis positioners. The alignment process, which is captured by a camera located above the DUT and a light source, is described in the following section.

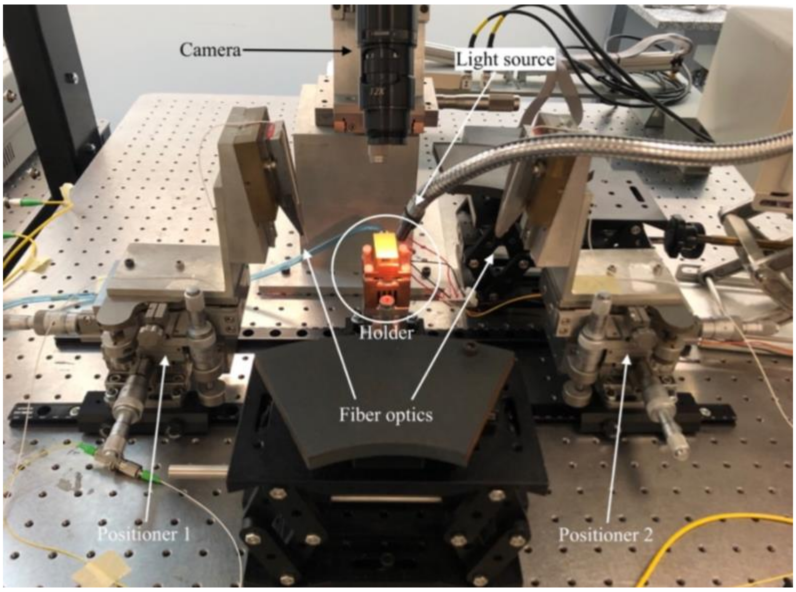

Fig. 44. Details of the components of the setup.

The power meter measures the power in dBm. The DUT was heated up and cooled down using a thermo-electric cooler (TEC). These devices leverage the Peltier effect present in junctions of different conductor materials. When a current flows through them, heating or cooling occurs at the junction. Temperature is adjusted with a laser diode controller that acts as a constant current source.

4.2. Passive characterization

The sample used for these measurements contains two add-drop rings, as well as some other not relevant structures. On the left, henceforth ring 1, we find a racetrack ring with total length L=30 µm and coupling length L_c=2 µm. On the right, henceforth ring 2, we find the structure we based 3.3 on: another racetrack ring resonator with L=42 µm and L_c=8 µm**.** Fig. 45 shows the physical design of the rings using KLayout [37], a layout viewer and editor. Fig. 46 shows one of the ring structures after placing the sample on the holder and obtaining a camera view.

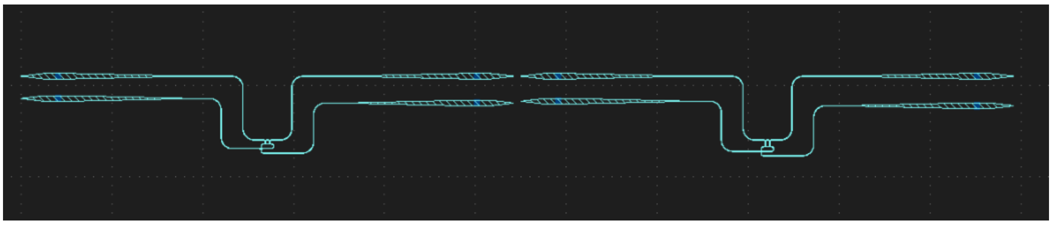

Fig. 45. Layout view of the sample. On the left: ring of 30µm (ring 1). On the right: ring of 42µm (ring 2).

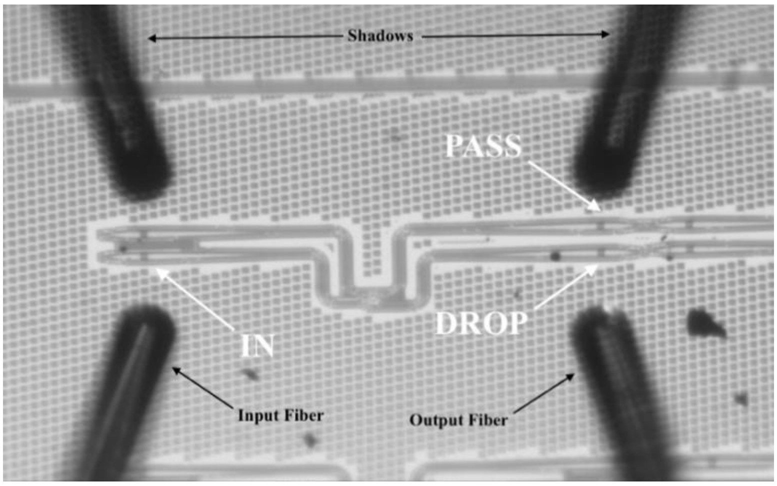

Fig. 46. View of the ring structure (center). Black images on both sides are input and output coupling fiber optics and their shadows.

The first step of the measurement process is the fiber alignment. By adjusting X, Y and Z positions of the fibers, input and output ports need to be aligned until the maximum output power is observed at the Power Meter. The coupling of light through fiber optics to the integrated structure is achieved via gratings. Gratings are sensitive to the polarization of light, meaning the polarization controller needs to be adjusted to obtain maximum output power. The typical response of a grating has maximum coupling efficiency (minimum losses) centered at 1550 nm. Nevertheless, fabrication deviations may shift this response towards lower or higher wavelengths.

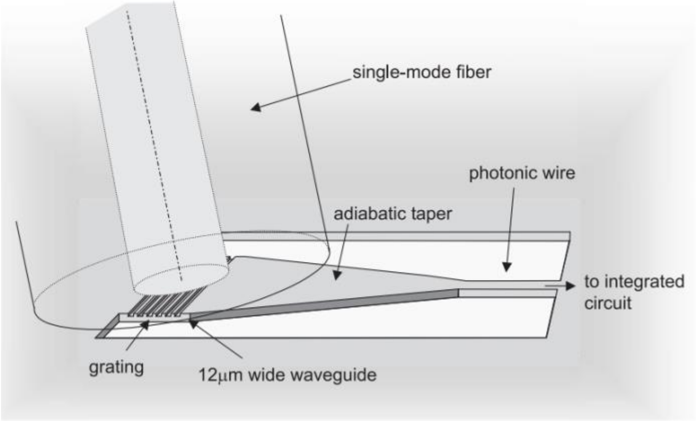

Fig. 47. Grating coupler between a fiber optic and a photonic waveguide [38].

Fig. 48 documents the appearance of aligned fibers. The correct height is achieved when fibers and their shadows are “touching” each other in the camera view. Alignment for the measurement of power at the Pass and Drop ports is different. Recalling the typical add-drop ring response (Fig. 27), at the Pass port, maximal power is obtained when the working wavelength is away from resonant points. At the Drop port we have the opposite scenario: maximal power is obtained at the resonant wavelengths. It is therefore necessary to adjust the laser’s wavelength before aligning the fibers.

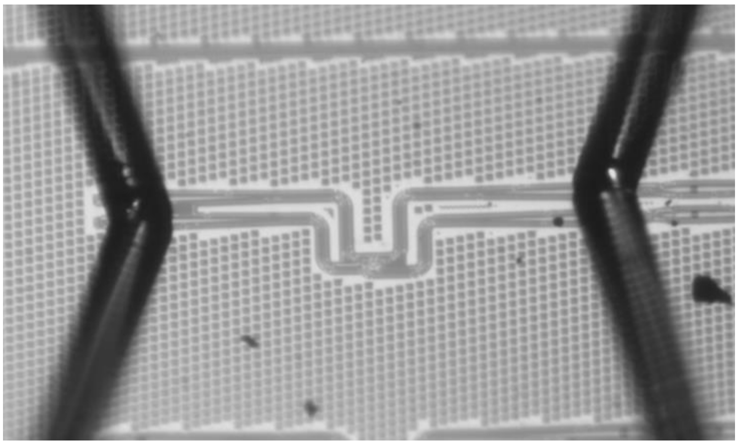

Fig. 48. Aligned fibers and view of the ring.

The goal of the passive characterization is to observe the response of the structures as a function of the wavelength at room temperature (25º C). The optical signal to be input into the rings has 0 dBm of power. A first coarse wavelength sweep is performed in order to locate the resonances. Fig. **49** presents the results. Resonances in the first ring appear at 1563.8 nm and 1583.2 nm. Resonances in the second ring appear at 1560 nm, 1573.75 nm and 1587.5 nm. The ascending characteristic is due to the response of the grating. A comparison between the measured FSR and the theoretical one is provided in Table **9**.

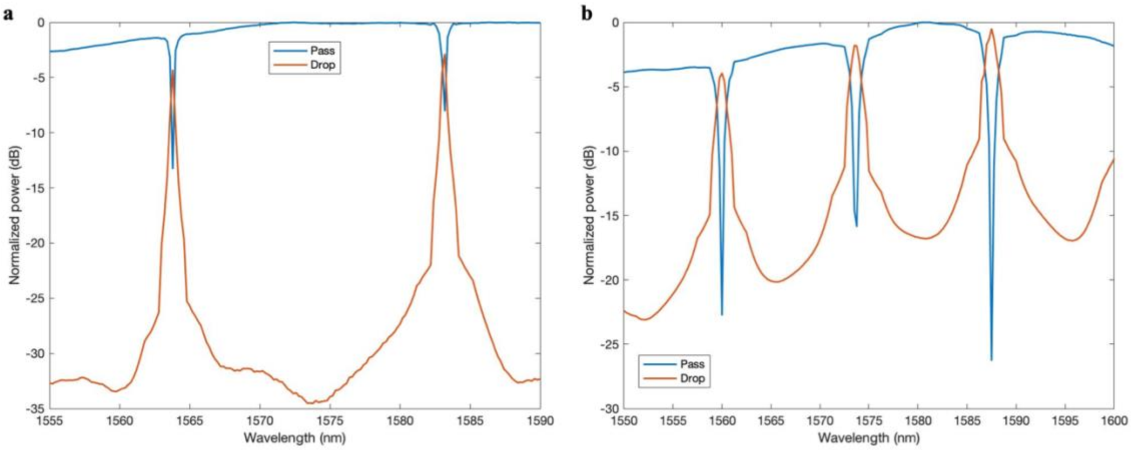

Fig. 49. Response of the rings as a function of the wavelength. FSR in **a)** ring 1 is bigger than in **b)** ring 2.

	Ring 1 (30µm) @1583.2 nm	**Ring 2 (42µm) @1587.5 nm**
Experimental FSR (nm)	19.40	13.75
Theoretical FSR (nm) [1]	19.29	13.72

Table 9. Experimental and theoretical FSR after the passive characterization.

The next step is to carry out a comparison of experimental results and simulations for resonances measured with a finer wavelength sweep. For that purpose, we adjust the coupling coefficients in order to obtain a fitting between both responses: experimental and simulation. The subsequent figures show the response at the Pass and Drop ports superimposed with simulations.

---

[1] Computed using Eq. (13).

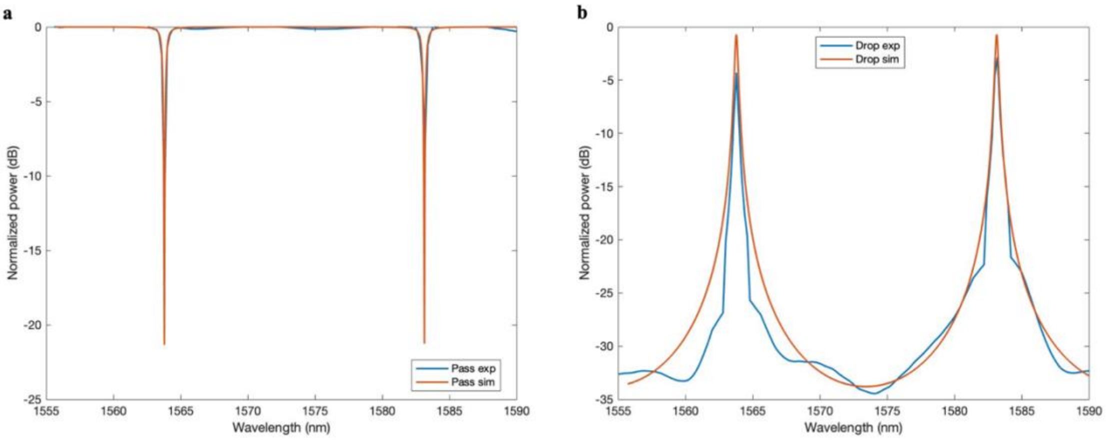

Fig. 50. Fitting of simulations to experimental results for ring 1. *K* obtained is 0.04.

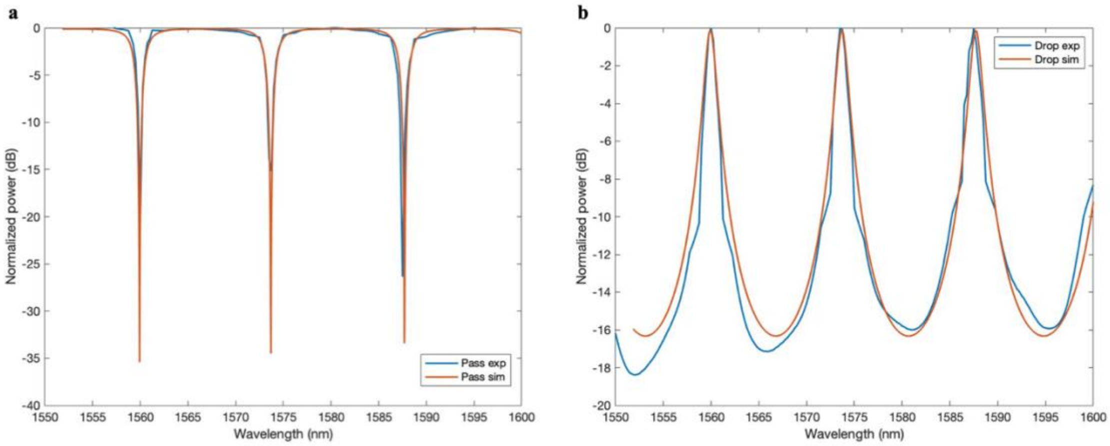

Fig. 51. Fitting of simulations to experimental results for ring 2. *K* obtained is 0.26.

In both rings the adjustments are in very good agreement. For the first ring, the computed coupling coefficient *K* is **0.04**. This matches the FTDT simulation results. For the second ring, resulting *K* is **0.26** which satisfactorily coincides with the optimal *K* designed in Section 3.3.

Finally, we analyze the potential performance of both rings if they were to be integrated with GST. Results for the second were derived in Section 3.3.These are found in Fig. 34 and Table 7 but are recalled here for comparison. The response of a ring of length 30 μm and coupling coefficients of 0.04 was simulated using MATLAB code found in Appendix 1.

	Ring 1 (L=30µm, K=0.04)	**Ring 2 (L=42µm, K=0.26)**
CT aGST (dB)	-14.43	-29.1324
CT cGST (dB)	-37.15	-20.6292
IL aGST (dB)	1.83	0.3126
IL cGST (dB)	0.13	0.9903
FWHM (nm)	0.32	1.41
FSR (nm)	19.07	13.715

Table 10. Comparison of resulting parameters yielded by both rings.

Even though response in crystalline state in ring 1 is superior, the value of insertion losses in amorphous state is not acceptable. Ring 2 offers a trade-off between switching states, as well as improving the bandwidth (FWHM). We therefore conclude that the optimal ring to deposit GST would be ring 2.

4.3. Thermo-optical characterization

The thermo-optical effect is the variation in the refractive index of an optical material with temperature [39]. The change of real (n) and imaginary parts (k) of the refractive index can be linearly approximated by [22]:

$$n(T_0 + \Delta T) \approx n_0 + \beta \Delta T \tag{22}$$

$$k(T_0 + \Delta T) \approx k_0 + \gamma \Delta T \tag{23}$$

where β and γ are the material thermo-optical coefficients. The change in n will result in a shift of the spectral response (see Eq. (3)) and the change in k will result in some attenuation (see Eq. (2)). In silicon waveguides, the effect of the variation of k is negligible ($\beta = 1.86 \cdot 10^{-4}$ /ºC, $\gamma = 0$). Therefore, only a phase shift will be observed.

The goal of the measurements is to observe the influence of the thermo-optical effect in the response of the two add-drop ring resonators based on Si waveguides outlined in Section 4.2. The measurement process entails the rising of the temperature employing the TEC described in Section 4.1. We first choose a resonant wavelength and set a 2 nm-wide window around it. In every iteration, temperature is increased in steps of 10ºC (**ΔT=10ºC**) and a shift of the resonant wavelength is measured. In an add-drop ring, the wavelength displacement depends only on the effective refractive variation (Δn_{eff}), the initial resonant wavelength (λ) and the group index (n_g). Therefore, dimensions of the ring are not impactful. We first present measurement results of ring 1 and later compare with ring 2 to prove it.

$$\Delta\lambda = \Delta n_{eff} \frac{\lambda_0}{n_g} \tag{24}$$

We focus on the resonance appearing at around 1563 nm (see Fig. 49 a). Power is normalized to the maximum. Gratings' response is rectified by subtracting the envelope to the response.

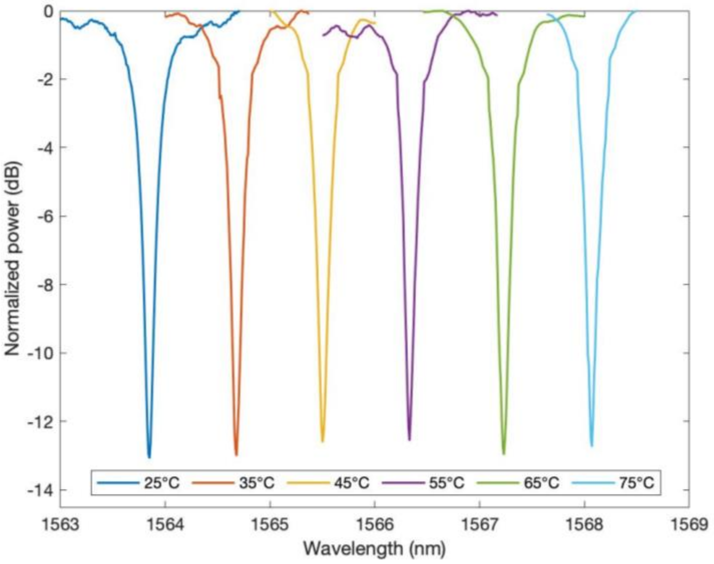

Fig. 52. Results of power measurements at the Pass port for different temperatures.

Temperature	Resonant Wavelength (nm)	Shift with respect to λ_0 (nm)
25ºC	1563.85	-
35ºC	1564.68	0.83
45ºC	1565.50	1.53
55ºC	1566.33	2.36
65ºC	1567.23	3.26
75ºC	1568.07	4.1

Table 11. Resonant wavelengths and shifts for different temperatures at the Pass port.

Next, response at the Drop port is analyzed. Again, we focus on the middle resonance and shift the sweep window as we increase the temperature. As expected, the resonant wavelengths and shifts are almost identical to the Pass port results.

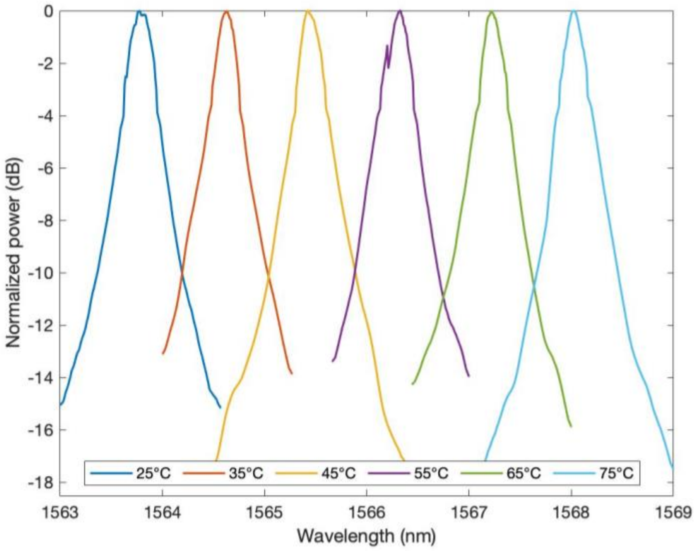

Fig. 53. Results of power measurements at the Drop port.

Temperature	Resonant Wavelength (nm)	Shift with respect to λ_0 (nm)
25ºC	1563.78	-
35ºC	1564.63	0.85
45ºC	1565.43	1.65
55ºC	1566.32	2.54
65ºC	1567.22	3.44
75ºC	1568.03	4.25

Table 12. Resonant wavelengths and shifts for different temperatures at the Drop port.

The same process is followed for ring 2. Fig. 54 shows the wavelength shift as a function of the temperature for both rings. The trend in both cases is very similar.

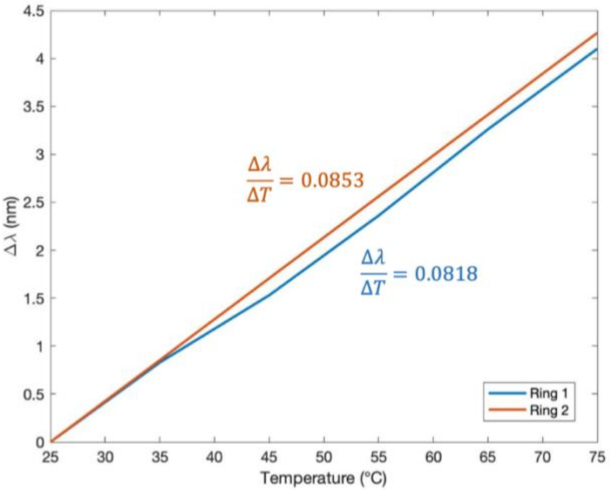

Fig. 54. Resonant wavelength shift as a function of temperature.

To conclude, the values of effective refractive index change computed using Equation (24) are presented. Resulting phase shift as a function of temperature of ring 1 is used for the computation. If we used results for ring 2 results would be very similar. The simulated effective refractive index change as a function of the temperature was also obtained using FemSIM. Fig. **55** shows a comparison between these values. A temperature increase of 50º C is needed in order to achieve a contrast of only 0.011. Thermo-optic effect in silicon is too slow for applications requiring fast switching speeds. A Si waveguide with GST can offer higher speeds and non-volatile switching performance. Short optical pulses could be used to drive the GST state so that no constant supply would be needed to maintain it. Integration of active materials like GST can therefore derive in ultra-compact switch devices with high performance.

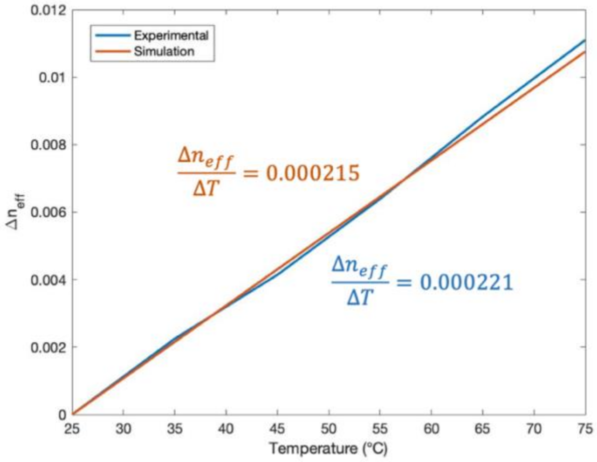

Fig. 55. Effective refractive index change as a function of temperature.

5. Conclusions and future work

The past decades have witnessed a frenetic and unparalleled development of electronics and integrated circuits. Already in 1965 with Moore’s Law it was predicted that the number of integrated electronic components in a chip would double every two years. More than 50 years later, it is still guiding the semiconductor industry in terms of planning and target setting. Computers are smaller and faster than ever. The throughput limiting factor is not the processing power but the delays in interconnections between components.

Integrated photonics is presented as a solution because it is a faster and less power-consuming platform, offering a significantly higher bandwidth compared to electronic systems. Photonics and optics have already transformed communications and will potentially do the same in other fields like imaging, sensing and computing applications. Nevertheless, the commercial excitement for the coming years lies preferentially in the potential integration of electronics and photonics rather than in the replacement of the former by the latter. A convergence between both domains by generating a task segmentation would be optimal [40].

Even though the level of integration of photonics is still behind electronics, the progress in the field has significantly advanced in the last decade [41]. Several impressive demonstrations of monolithic integration of photonics and electronics have been reported. The fabrication of a single chip integrating over 70 million transistors and 850 photonic components was demonstrated by using a commercial high-performance 45-nm CMOS node process [42]. More recently, the integration of photonics with electronics fabricated in a 65-nm CMOS node process to develop multi-wavelength optical transceivers was also demonstrated [43]. The transceiver achieved a bandwidth density of 180 Gbit/s·mm^{-2} with 10% of the effective area occupied by photonics.

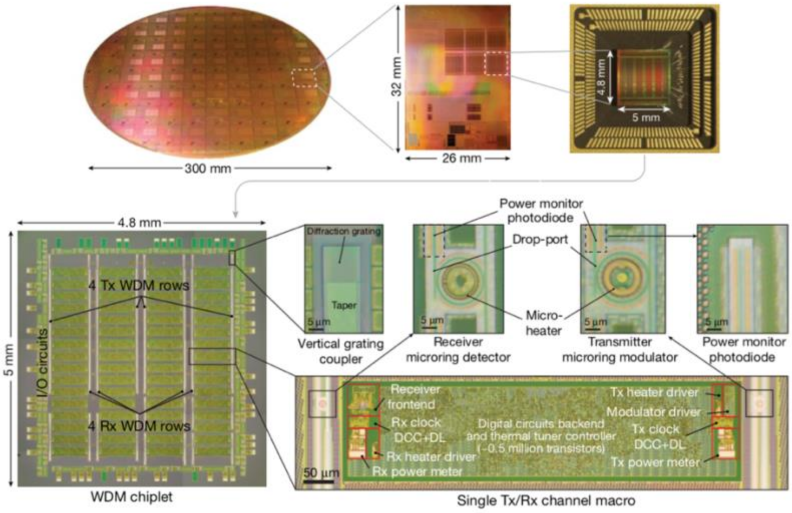

Fig. 56. Example of monolithic electronic–photonic platform in 65-nm bulk CMOS [43].

Photonics is a reality and moving from the long-distance communications domain to chip-to-chip links and on-chip applications. The all-optical storage and processing of data is proposed to circumvent the energy and time-consuming optical-electrical signal conversions [44]. Phase-Change Materials, due to their unique properties described throughout this work, are expected to play a key role in this purpose and in the future commercialization and mass-production of photonic circuits. The synergy between PCMs and integrated photonics is resulting in revolutionary breakthroughs. On-chip non-volatile memories [13], [45], all-optical switches [15], [36], optical computing [46], modulators [14], [24], [25] and neuromorphic computing [29], [30] have already been demonstrated due to the employment of these materials, thus making the all-optical prospect closer than ever.

Especially outstanding is the non-volatile property of some PCMs that offers significant potential advancements in terms of level of integration and in the fields of optical memories and all-photonic computation. One of the most widely used non-volatile PCMs is GST. Its fast transition between amorphous and crystalline phases, the high difference in optical properties between them and the self-holding feature make GST appropriate and best suited for many applications. Nevertheless, temperatures needed to induce the state transition are quite high (~600ºC in comparison to the ~65ºC needed for VO_2) which may hinder its implementation. A thoughtful control of the manufacturing process and the state change technique is essential. GST has only recently been employed in photonic applications, so research on this material and how to overcome the constraints that it presents is still needed. In particular, the homogenization of the values of refractive index of GST may be particularly helpful. As seen in Section 3.1, these values strongly depend on the fabrication process and discrepancies are found in the literature. It would be valuable to adapt this process so minimal losses in both states could be attained on every occasion.

In this work, the employment of GST to implement switching devices based on ring resonators and Mach-Zehnder interferometers was examined. Results show that, in the case of the ring, the integration of GST does not have a huge impact in terms of size/footprint but does significantly improve the performance. In the case of the MZI, the employment of GST allows for ultracompact devices, but losses in both states, especially in the crystalline state, hamper its practical application in devices. The employment of GSST (showing much lower losses) may be further investigated as a potential solution.

As a continuation of this work, several proposals are suggested. These include the manufacturing of samples including MZI structures to validate the theoretical design developed in Section **Error! Reference source not found.** and the experimental deposition of GST. The easiest way to induce the phase change of GST is by heating the sample in an oven and subsequently performing the pertinent measurements. Other approaches based on optical pulses with relatively high power [13] have also been reported. Nevertheless, in this work we propose a new and promising technique: by rising the temperature of the sample on the holder using the TEC and combining it with optical pulses to control the GST state change, the energy of these pulses could be reduced therefore minimizing the power consumption. We encourage future research to develop this approach.

In conclusion, Phase-Change Materials and particularly GST are expected to play a major role in the short and long-term development of integrated photonics based on silicon photonics, opening up the field to promising applications.

6. References

[1] G. Lifante, “Introduction to Integrated Photonics,” 2005, pp. 1–23.

[2] A. Physics, A. Physics, O. If, and B. Publications, *Topics in Applied Physics Volume 101 Topics in Applied Physics*, vol. 101. 2006.

[3] L. Thylén and L. Wosinski, “Integrated photonics in the 21st century,” *Photonics Res.*, vol. 2, no. 2, p. 75, 2014.

[4] G. N. Malheiros-Silveira, F. Lu, I. Bhattacharya, T. T. D. Tran, H. Sun, and C. J. Chang-Hasnain, “III-V Compound Semiconductor Nanopillars Monolithically Integrated to Silicon Photonics,” *ACS Photonics*, vol. 4, no. 5, pp. 1021–1025, 2017.

[5] X. Chen *et al.*, “The Emergence of Silicon Photonics as a Flexible Technology Platform,” *Proc. IEEE*, vol. 106, no. 12, pp. 2101–2116, 2018.

[6] Syms, R. R. A. (1994). Silica-on Silicon Integrated Optics. In S. Martellucci, A. N. Chester, & M. Bertolotti (Eds.), Advances in Integrated Optics (pp. 121–150).

[7] R. Soref, “The Achievements and Challenges of Silicon Photonics,” *Adv. Opt. Technol.*, vol. 2008, pp. 1–7, 2008.

[8] K. J. Miller, R. F. Haglund, and S. M. Weiss, “Optical phase change materials in integrated silicon photonic devices: review,” *Opt. Mater. Express*, vol. 8, no. 8, p. 2415, 2018.

[9] Q. Wang *et al.*, “1.7 Gbit/in.2 gray-scale continuous-phase-change femtosecond image storage,” *Appl. Phys. Lett.*, vol. 104, no. 12, pp. 12–14, 2014.

[10] M. Wuttig and N. Yamada, “Phase-change materials for rewriteable data storage,” *Nat. Mater.*, vol. 6, no. 11, pp. 824–832, 2007.

[11] M. Wuttig, H. Bhaskaran, and T. Taubner, “Phase-change materials for non-volatile photonic applications,” *Nat. Photonics*, vol. 11, no. 8, pp. 465–476, 2017.

[12] Z. Yang and S. Ramanathan, “Breakthroughs in photonics 2014: Phase change materials for photonics,” *IEEE Photonics J.*, vol. 7, no. 3, pp. 1–5, 2015.

[13] C. Rios *et al.*, “Integrated all-photonic non-volatile multi-level memory,” *Nat. Photonics*, vol. 9, no. 11, pp. 725–732, 2015.

[14] Z. Yu, J. Zheng, P. Xu, W. Zhang, and Y. Wu, “Ultracompact electro-optical modulator-based Ge2Sb2Te5 on Silicon,” *IEEE Photonics Technol. Lett.*, vol. 30, no. 3, pp. 250–253, 2018.

[15] Q. Zhang, Y. Zhang, J. Li, R. Soref, T. Gu, and J. Hu, “Broadband nonvolatile

photonic switching based on optical phase change materials: beyond the classical figure-of-merit," *Opt. Lett.*, vol. 43, no. 1, p. 94, 2018.

[16] Zhang, Y., Li, J., Chou, J., Fang, Z., Yadav, A., Lin, H., … Hu, J. (2017). Broadband Transparent Optical Phase Change Materials. Conference on Lasers and Electro-Optics, JTh5C.4.

[17] "Birth of the programmable optical chip," *Nat. Photonics*, vol. 10, no. 1, pp. 1–1, 2016.

[18] Pérez, D., Gasulla, I., Crudgington, L., Thomson, D. J., Khokhar, A. Z., Li, K., … Capmany, J. (2017). Multipurpose silicon photonics signal processor core. Nature Communications, 8(1), 636.

[19] P. Xu, J. Zheng, J. K. Doylend, and A. Majumdar, "Low-Loss and Broadband Nonvolatile Phase-Change Directional Coupler Switches," *ACS Photonics*, vol. 6, no. 2, pp. 553–557, 2019.

[20] C. Wu, H. Yu, H. Li, X. Zhang, I. Takeuchi, and M. Li, "Low-Loss Integrated Photonic Switch Using Subwavelength Patterned Phase Change Material," *ACS Photonics*, vol. 6, no. 1, pp. 87–92, Jan. 2019.

[21] J. Zheng *et al.*, "GST-on-silicon hybrid nanophotonic integrated circuits: a non-volatile quasi-continuously reprogrammable platform," *Opt. Mater. Express*, vol. 8, no. 6, p. 1551, 2018.

[22] M. Stegmaier, C. RÍos, H. Bhaskaran, and W. H. P. Pernice, "Thermo-optical Effect in Phase-Change Nanophotonics," *ACS Photonics*, vol. 3, no. 5, pp. 828–835, 2016.

[23] G. T. Reed, G. Mashanovich, F. Y. Gardes, and D. J. Thomson, "Silicon optical modulators," *Nat. Photonics*, vol. 4, no. 8, pp. 518–526, 2010.

[24] R. M. Briggs, I. M. Pryce, and H. A. Atwater, "Compact silicon photonic waveguide modulator based on the vanadium dioxide metal-insulator phase transition," *Opt. Express*, vol. 18, no. 11, p. 11192, 2010.

[25] H. Liang, R. Soref, J. Mu, A. Majumdar, X. Li, and W. P. Huang, "Simulations of Silicon-on-Insulator Channel-Waveguide Electrooptical 2 x 2 Switches and 1 x 1 Modulators Using a Ge 2 Sb 2 Te 5 Self-Holding Layer," *J. Light. Technol.*, vol. 33, no. 9, pp. 1805–1813, 2015.

[26] I. Olivares *et al.*, "Optical switching in hybrid VO2/Si waveguides thermally triggered by lateral microheaters," *Opt. Express*, vol. 26, no. 10, pp. 12387–12395, May 2018.

[27] L. Wang, S. R. Lu, and J. Wen, "Recent Advances on Neuromorphic Systems Using Phase-Change Materials," *Nanoscale Res. Lett.*, vol. 12, no. 1, 2017.

[28] A. Sebastian, M. Le Gallo, G. W. Burr, S. Kim, M. Brightsky, and E. Eleftheriou, “Tutorial: Brain-inspired computing using phase-change memory devices,” *J. Appl. Phys.*, vol. 124, no. 11, 2018.

[29] Y. Shen, N. C. Harris, D. Englund, and M. Soljacic, “Deep learning with coherent nanophotonic circuits,” *2017 5th Berkeley Symp. Energy Effic. Electron. Syst. E3S 2017 - Proc.*, vol. 2018-Janua, no. July, pp. 1–2, 2018.

[30] H. Bhaskaran, W. H. P. Pernice, Z. Cheng, C. Ríos, and C. D. Wright, “On-chip photonic synapse,” *Sci. Adv.*, vol. 3, no. 9, p. e1700160, 2017.

[31] S. R. Nandakumar, M. Le Gallo, I. Boybat, B. Rajendran, A. Sebastian, and E. Eleftheriou, “A phase-change memory model for neuromorphic computing,” *J. Appl. Phys.*, vol. 124, no. 15, pp. 1–12, 2018.

[32] J. Song, S. Ghosh, N. Dhingra, H. Zhang, L. Zhou, and B. M. A. Rahman, “Feasibility study of a Ge 2 Sb 2 Te 5 -clad silicon waveguide as a non-volatile optical on-off switch,” *OSA Contin.*, vol. 2, no. 1, p. 49, 2019.

[33] H. Zhang *et al.*, “Ultracompact Si-GST hybrid waveguides for nonvolatile light wave manipulation,” *IEEE Photonics J.*, vol. 10, no. 1, pp. 1–10, 2018.

[34] “FemSIM - Generalized Mode Solver - Finite Element Method.” [Online]. Available: https://www.synopsys.com/optical-solutions/rsoft/passive-device-femsim.html. [Accessed: 25-Jun-2019].

[35] L. Chrostowski and M. Hochberg, *Silicon Photonics Design*. Cambridge: Cambridge University Press, 2015.

[36] Sanchez, L., Lechago, S., Gutierrez, A., & Sanchis, P. (2016). Analysis and Design Optimization of a Hybrid VO2/Silicon 2x2 Microring Switch. IEEE Photonics Journal, 8(2), 1–9.

[37] “KLayout Layout Viewer And Editor.” [Online]. Available: https://www.klayout.de/. [Accessed: 27-Jun-2019].

[38] Taillaert, D., Van Laere, F., Ayre, M., Bogaerts, W., Van Thourhout, D., Bienstman, P., & Baets, R. (2006). Grating Couplers for Coupling between Optical Fibers and Nanophotonic Waveguides. Japanese Journal of Applied Physics, 45, 6071–6077.

[39] “Thermo-Optic Coefficients,” *Handb. Opt. Constants Solids*, pp. 115–261, Jan. 1997.

[40] R. Kirchain and L. Kimerling, “A roadmap for nanophotonics,” *Nat. Photonics*, vol. 1, no. 6, pp. 303–305, 2007.

[41] K. A. Williams, "Prospects for Electronic Photonic Integration," in Advanced

Photonics 2017 (IPR, NOMA, Sensors, Networks, SPPCom, PS), OSA Technical Digest (online) (Optical Society of America, 2017), paper IW3A.1.

[42] Sun, C. et al., "Single-chip microprocessor that communicates directly using light," Nature 528, 534-538 (2015).

[43] Atabaki, A. H., et al., "Integrating photonics with silicon nanoelectronics for the next generation of systems on a chip," Nature 556, 349-354 (2018).

[44] C. D. Wright *et al.*, “Integrated Phase-change Photonics: A Strategy for Merging Communication and Computing,” in *Optical Fiber Communication Conference (OFC) 2019*, 2019, p. M1D.3.

[45] C. Rios, P. Hosseini, C. D. Wright, H. Bhaskaran, and W. H. P. Pernice, “On-chip photonic memory elements employing phase-change materials,” *Adv. Mater.*, vol. 26, no. 9, pp. 1372–1377, 2014.

[46] C. Sun *et al.*, “Single-chip microprocessor that communicates directly using light,” *Nature*, vol. 528, no. 7583, pp. 534–538, 2015.

Appendix 1: MatLab code

```
%ADD-DROP RING RESONATOR DESIGN

Clf

resolution=1e-12; %1pm
wl=1540e-9:resolution:1575e-9; %wavelength

% Effective refractive index: derived by doing a parametric analysis on the waveguide
neff_Si=-1.1850*1e6*wl+4.2246;
neff_aGST=-0.9442*1e6*wl+4.0475;
neff_cGST=-0.7839*1e6*wl+4.0692;

%Losses
a_SidB=10; %dB/cm
a_aGSTdB=0.0195; %dB/microm
a_cGSTdB=5.5307; %dB/microm
%Transform into Np/m
a_Si=a_SidB*1e2/(10*log10(exp(1)));
a_aGST=a_aGSTdB*1e6/(10*log10(exp(1)));
a_cGST=a_cGSTdB*1e6/(10*log10(exp(1)));

%Length
L=42e-6;
L_GST=2.87e-6;
L_Si=L-L_GST;

%Coupling coefficients
K1=0.26;
K2=0.26;
t1=sqrt(1-K1); %Self-coupling coefficient
k1=sqrt(K1); %Cross-coupling coefficient
t2=sqrt(1-K2);
k2=sqrt(K2);

res_wl=zeros(1,2);

for i=1:2
    if i==1 %Amorphous state

        %Losses will change depending on the state of GST
        A=exp(-a_Si*L_Si-a_aGST*L_GST);
        phi=(2*pi./wl).*(neff_Si*L_Si+neff_aGST*L_GST);

    else %Crystalline state

        A=exp(-a_Si*L_Si-a_cGST*L_GST);
        phi=(2*pi./wl).*(neff_Si*L_Si+neff_cGST*L_GST);
```

```
    end
    %Transfer function expression
    Epass=(t1-conj(t2)*sqrt(A)*exp(1j*phi))./(1-
sqrt(A)*conj(t1)*conj(t2)*exp(1j*phi));
    Edrop=(-conj(k1)*k2*A^0.25*exp(1j*phi/2))./(1-
sqrt(A)*conj(t1)*conj(t2)*exp(1j*phi));

    %Power calculation
    Ppass=10*log10(abs(Epass).^2);
    Pdrop=10*log10(abs(Edrop).^2);

    %Representation
    plot(wl/1e-9,Ppass,'-','LineWidth',1.5)
    hold on
    plot(wl/1e-9,Pdrop,'-','LineWidth',1.5)
    xlabel('Wavelength (nm)')
    ylabel('Output power (dB)')
    set(gca,'FontSize',11);
    xlim([1540 1575])

end
legend('P_p_a_s_s_ aGST','P_d_r_o_p aGST','P_p_a_s_s_ cGST','P_d_r_o_p
cGST')
```

```
%2x2 MZI DESIGN

resolution=1e-12; %1pm
wl=1540e-9:resolution:1560e-9; %wavelength

%Effective refractive index: derived by doing a parametric analysis on
the waveguide
neff_Si=-1.1850*1e6*wl+4.2246;
neff_aGST=-0.9442*1e6*wl+4.0475;
neff_cGST=-0.7839*1e6*wl+4.0692;

%Losses
a_SidB=10; %dB/cm
a_aGSTdB=0.0195; %dB/microm
a_cGSTdB=5.5307; %dB/microm
%Transform into Np/m
a_Si=a_SidB*1e2/(20*log10(exp(1)));
a_aGST=a_aGSTdB*1e6/(20*log10(exp(1)));
a_cGST=a_cGSTdB*1e6/(20*log10(exp(1)));

%Length (symmetrical MZI)
L=10e-6;
L_GST=2.87e-6;
L_Si=L-L_GST;
```

```
%Propagation constant
B_Si=neff_Si*2*pi./wl;
B_aGST=neff_aGST*2*pi./wl;
B_cGST=neff_cGST*2*pi./wl;

%Coupling coefficients
Ki=0.7455; Ko=0.5;

%Matrices to be used in the transfer function
A=[sqrt(1-Ko) -1j*sqrt(Ko); -1j*sqrt(Ko) sqrt(1-Ko)];
C=[sqrt(1-Ki) -1j*sqrt(Ki); -1j*sqrt(Ki) sqrt(1-Ki)];

%Input field
Ei=[1;0];

aux=zeros(2,2); %Auxiliar matrix to store results
Eo1=zeros(1,length(wl));
Eo2=zeros(1,length(wl));

for i=1:length(wl)
    aux=A*[exp(-a_Si*L_Si-
a_aGST*L_GST)*exp(1j*(B_Si(i)*L_Si+B_aGST(i)*L_GST)) 0; 0 exp(-
a_Si*L_Si-a_cGST*L_GST)*exp(1j*(B_Si(i)*L_Si+B_cGST(i)*L_GST))]*C*Ei;
    Eo1(i)=aux(1);
    Eo2(i)=aux(2);
end

%Power calculation
Po1=10*log10(abs(Eo1).^2);
Po2=10*log10(abs(Eo2).^2);

%Representation
figure
plot(wl/1e-9,Po1,'lineWidth',2)
hold on
plot(wl/1e-9,Po2,'lineWidth',2)
legend('Po1','Po2')
xlabel('Wavelength (nm)')
ylabel('Po/Pi (dB)')
set(gca,'FontSize',12)
```